



**HAL**  
open science

## Collective magnetotaxis of microbial holobionts is optimized by the three-dimensional organization and magnetic properties of ectosymbionts

Daniel M Chevrier, Amélie Juhin, Nicolas Menguy, Romain Bolzoni, Paul E. D. Soto-Rodriguez, Mila Kojadinovic-Sirinelli, Greig A. Paterson, Rachid Belkhou, Wyn Williams, Fériel Skouri-Panet, et al.

### ► To cite this version:

Daniel M Chevrier, Amélie Juhin, Nicolas Menguy, Romain Bolzoni, Paul E. D. Soto-Rodriguez, et al.. Collective magnetotaxis of microbial holobionts is optimized by the three-dimensional organization and magnetic properties of ectosymbionts. *Proceedings of the National Academy of Sciences of the United States of America*, 2023, 120 (10), pp.e2216975120. 10.1073/pnas.2216975120 . hal-04014315

**HAL Id: hal-04014315**

**<https://hal.science/hal-04014315>**

Submitted on 3 Mar 2023

**HAL** is a multi-disciplinary open access archive for the deposit and dissemination of scientific research documents, whether they are published or not. The documents may come from teaching and research institutions in France or abroad, or from public or private research centers.

L'archive ouverte pluridisciplinaire **HAL**, est destinée au dépôt et à la diffusion de documents scientifiques de niveau recherche, publiés ou non, émanant des établissements d'enseignement et de recherche français ou étrangers, des laboratoires publics ou privés.

1 **Collective magnetotaxis of microbial holobionts is optimized by the three-**  
2 **dimensional organization and magnetic properties of ectosymbionts**

3 Daniel M. Chevrier<sup>1\*</sup>, Amélie Juhin<sup>2</sup>, Nicolas Menguy<sup>2</sup>, Romain Bolzoni<sup>1</sup>, Paul E. D. Soto-Rodriguez<sup>1</sup>,  
4 Mila Kojadinovic-Sirinelli<sup>1</sup>, Greig A. Paterson<sup>3</sup>, Rachid Belkhou<sup>4</sup>, Wyn Williams<sup>5</sup>, Fériel Skouri-Panet<sup>2</sup>,  
5 Artemis Kosta<sup>6</sup>, Hugo Le Guenno<sup>6</sup>, Eva Pereiro<sup>7</sup>, Damien Faivre<sup>1</sup>, Karim Benzerara<sup>2</sup>, Caroline L. Monteil<sup>1</sup>,  
6 Christopher T. Lefevre<sup>1\*</sup>

7

8 <sup>1</sup>Aix-Marseille Université, CNRS, CEA, UMR7265, BIAM, Saint-Paul-lez-Durance 13108, France

9 <sup>2</sup>Sorbonne Université, UMR CNRS 7590, MNHN, IRD, Institut de Minéralogie, de Physique des Matériaux  
10 et de Cosmochimie, IMPMC, 75005, Paris, France

11 <sup>3</sup>Department of Earth, Ocean and Ecological Sciences, University of Liverpool, L69 7ZE, Liverpool, UK

12 <sup>4</sup>Synchrotron Soleil, L'Orme des Merisiers, Saint-Aubin -BP 48, 91192 Gif-sur-Yvette Cedex, France

13 <sup>5</sup>University of Edinburgh, School of GeoSciences, Grant Institute, West Mains Road, Edinburgh EH9 3JW

14 <sup>6</sup>Plateforme de Microscopie de l'Institut de Microbiologie de la Méditerranée, IMM, Institut de  
15 Microbiologie, FR3479, Campus CNRS, 13402 Marseille cedex 20, France

16 <sup>7</sup>ALBA Synchrotron Light Source, Cerdanyola del Vallés, Barcelona 08290, Spain

17

18 **\*Corresponding authors:** Drs. Daniel Chevrier and Christopher T. Lefevre

19 **Emails:** daniel.chevrier@cea.fr and christopher.lefevre@cea.fr

20

21 **ORCID:** Daniel M. Chevrier (0000-0002-0914-6714), Amélie Juhin (0000-0003-0752-3034), Nicolas  
22 Menguy (0000-0003-4613-2490), Romain Bolzoni (0000-0002-5741-3856), Paul E. D. Soto-Rodriguez  
23 (0000-0002-2425-932X), Mila Kojadinovic-Sirinelli (0000-0001-8110-3113), Greig A. Paterson (0000-  
24 0002-6864-7420), Rachid Belkhou (0000-0002-2218-7481), Wyn Williams (0000-0001-9210-7574),  
25 Fériel Skouri-Panet (0000-0002-2623-9058), Artemis Kosta (0000-0001-7115-4566), Hugo Le Guenno  
26 (0000-0003-1768-1212), Eva Pereiro (0000-0001-7626-5935), Damien Faivre (0000-0001-6191-3389),  
27 Karim Benzerara (0000-0002-0553-0137), Caroline L. Monteil (0000-0002-2834-6834), Christopher T.  
28 Lefevre (0000-0002-1692-0245).

29

30 **Author contributions:** D.M.C., A.J., N.M., D.F. K.B., C.L.M., and C.T.L. designed research; D.M.C.,  
31 A.J., N.M., K.B., Ro.B., W.W., G.A.P., M.K.S., P.E.D.S.R., and C.T.L. performed research; F.S.P., Ra.B.,  
32 D.F., A.K., H.L.G., and E.P. contributed new reagents/analytic tools; D.M.C., A.J., N.M., K.B., P.E.D.S.R.  
33 and C.T.L. analyzed data; D.M.C., C.L.M., and C.T.L. wrote the paper; N.M., P.E.D.S.R., G.A.P., D.F. and  
34 K.B. contributed partial writing.

35

36 The authors declare no competing interest.

37 **Classification:** Biological Sciences (Major), Biophysics and Computational Biology (Minor)

38

39 **Keywords:** collective magnetotaxis, magnetosomes, symbiosis, biomineralization, holobiont,  
40 magnetotactic bacteria

41

## 42 **Abstract**

43 Over the last few decades, symbiosis and the concept of holobiont – a host entity with a population of  
44 symbionts – have gained a central role in our understanding of life functioning and diversification.  
45 Regardless of the type of partner interactions, understanding how the biophysical properties of each  
46 individual symbiont and their assembly may generate collective behaviors at the holobiont scale remains a  
47 fundamental challenge. This is particularly intriguing in the case of the newly discovered magnetotactic  
48 holobionts (MHB) whose motility relies on a collective magnetotaxis (*i.e.*, a magnetic field-assisted motility  
49 guided by a chemo-aerotaxis system). This complex behavior raises many questions regarding how  
50 magnetic properties of symbionts determine holobiont magnetism and motility. Here, a suite of light-,  
51 electron- and X-ray-based microscopy techniques (including X-ray magnetic circular dichroism (XMCD))  
52 reveals that symbionts optimize the motility, the ultrastructure and the magnetic properties of MHBs from  
53 the microscale to the nanoscale. In the case of these magnetic symbionts, the magnetic moment transferred  
54 to the host cell is in excess ( $10^2$ - $10^3$  times stronger than free-living magnetotactic bacteria), well above the  
55 threshold for the host cell to gain a magnetotactic advantage. The surface organization of symbionts is  
56 explicitly presented herein, depicting bacterial membrane structures that ensure longitudinal alignment of  
57 cells. Magnetic dipole and nanocrystalline orientations of magnetosomes were also shown to be consistently  
58 oriented in the longitudinal direction, maximizing the magnetic moment of each symbiont. With an  
59 excessive magnetic moment given to the host cell, the benefit provided by magnetosome biomineralization  
60 beyond magnetotaxis can be questioned.

61

## 62 **Significance Statement**

63 Symbiosis between a motile microeukaryotic host and dozens of non-motile, surface-attached magnetic  
64 bacterial symbionts was recently discovered, where the host acquires geomagnetic field-guided navigation  
65 thanks to chains of ferrimagnetic nanoparticles (within organelles called magnetosomes) produced by the  
66 bacteria. Our findings reveal magnetic dipoles of each magnetosome chain consistently align and thus  
67 efficiently confer a large magnetic moment to the host cell. Remarkably, the calculated magnetic moment  
68 is greatly in excess of that required to gain a magnetotactic advantage. These results show an optimization

69 of collective magnetotaxis during the course of evolution owing to the three-dimensional organization and  
70 magnetic properties of bacteria but also raise the question on the magnetosome's function beyond magnetic  
71 field guidance since they abundantly cover the host.

72

### 73 **Introduction**

74 Species are adapted to their environment thanks to the heritable changes in their structure, physiology,  
75 locomotion, dispersal, reproduction and other behaviors that have passed the filter of natural selection over  
76 generations. Several evolutionary forces may trigger these changes and shape biodiversity, among which  
77 symbiosis has gained a lot of recognition in recent decades (1). By creating intimate and long-term physical  
78 interactions, different organisms may rapidly acquire a variety of functions, ranging from detoxification, to  
79 cell defense, motility and, in most cases, metabolic abilities. Together, symbiotic microorganisms form a  
80 single ecological unit, called a holobiont (2), whose functioning allows its partners/bionts to extend their  
81 ecological niche and colonize otherwise previously inaccessible habitats. The symbiont integration level  
82 may vary from a simple attachment to cell surfaces to their integration into the cell cytoplasm. In the most  
83 extreme cases of endosymbiont host integration, symbiosis can even lead to the creation of new organelles  
84 and genome transfer to the host nucleus, often illustrated by the eukaryogenesis (3, 4).

85 Symbioses are established between organisms from all domains of life and have been mostly  
86 studied in macrobial systems involving multicellular eukaryote models (5, 6). Symbioses in the microbial  
87 world are also widespread but less known even though they are of prime interest to gain insights into the  
88 mechanisms driving life complexification and evolution. However, observation and characterization of  
89 microbial symbioses have been challenging for many years; most symbionts defy commonly applied  
90 enrichment and cultivation techniques (1). Even if metagenomic and single-cell genomic approaches may  
91 now circumvent some of these issues by enabling the reconstruction of genomes from symbionts in their  
92 natural habitats (7), *in silico* approaches do not entirely reveal the holobiont structure and behavior.  
93 Therefore, interrogating the physical properties of microbial symbiotic systems may bring insights on  
94 mechanisms or interactions that have shaped biodiversity. Improvements in micro- and nano-scale  
95 analytical instrumentation and sample preparation strategies over the past few years have boosted  
96 biophysical research, permitting microbial holobiont studies from the single cell level to organelle level (8).  
97 For instance, approaches such as synchrotron-based X-ray spectromicroscopy imaging, focused ion beam  
98 (FIB)-scanning electron microscopy, and cryo electron microscopy (and associated cryo-preparation  
99 protocols) have made it possible to rigorously examine the ultrastructure and organization of individual

100 cells, while other techniques such as nanoscale secondary ion mass spectrometry (NanoSIMS) can trace the  
101 metabolic exchanges to decipher intra-/inter-cellular chemical interactions (9).

102           Microbial holobionts may adopt behavior patterns almost completely determined by the symbionts.  
103 Cell to cell interactions between bionts generate an emergent collective behavior that may change the  
104 mechanical, biological and physicochemical properties of each partner over generations. Although debated  
105 amongst evolutionary biologists (10, 11), a microbial holobiont can nevertheless be seen as a main unit of  
106 selection. As such, any cell or organelle function, structure and organization optimizing the collective  
107 behavior may therefore be selected in a given environmental context. These evolutionary processes may  
108 create a complete dependency in some biological systems, which is well illustrated by mitochondria and  
109 chloroplast evolution (12). Not all symbioses are obligatory, but most of them involve a metabolic  
110 dependency from at least one of the partners. Such is the case with the endosymbiotic methanogenic archaea  
111 or denitrifying bacteria in hydrogenosome-bearing protists (13, 14). Other benefits can rely on structural  
112 integrity or locomotion. Indeed, similar to other biological systems (15), symbiont interactions can generate  
113 a collective motion. For example, some flagellates are mobile owing to thousands of ectosymbiotic bacteria  
114 (*e.g.*, spirochetes) anchored to the host membrane, which ensure its movement with their flagella (16).

115           Recently, a new collective behavior was described in a group of microbial holobionts ubiquitous in  
116 anoxic marine sediments. The functioning of this holobiont relies on a multi-scale cooperation between a  
117 flagellate, euglenozoan protist and dozens of non-flagellated, sulfate-reducing bacteria of the  
118 *Deltaproteobacteria* class, which biomineralize magnetic nanocrystals (17). First, the host and symbionts  
119 interdependency relies on metabolic exchanges. Some of them were identified based on the host  
120 ultrastructure and ectosymbiont genome (17). Their syntrophy is most likely based on the transfer of  
121 molecular hydrogen produced by mitochondria-derived organelles, called hydrogenosomes, from the host  
122 to the bacteria that use it to reduce sulfate. Second, these holobionts harbor a peculiarity compared to other  
123 symbiotic systems described in such habitats: they adopt a collective magnetotaxis, (*i.e.*, a motility guided  
124 by a chemo-aerotaxis system and geomagnetic fields). Similar to magnetotactic bacteria (MTB) (18, 19),  
125 magnetotactic holobiont (MHB) motility is guided by geomagnetic fields, which is assumed to facilitate  
126 their positioning in preferred ecological niches, just below the oxic-anoxic boundaries of sediments. The  
127 passive alignment in a magnetic field is ensured by ectosymbionts through the biomineralization of chained  
128 lipidic vesicle-encapsulated ferrimagnetic nanocrystals called magnetosomes. Experimental observations  
129 evidenced that the magnetic guidance was influenced by oxygen gradients, while a nearly complete genome  
130 of biomineralizing bacteria showed complete loss of sensing and motility machinery (17). Therefore,  
131 magnetotaxis appears to emerge from the collective effects of magnetosome chain positioning from  
132 ectosymbiotic bacteria and the host motility and chemo-aerotaxis.

133

134           The discovery of MHBs raises many questions regarding the magnetic properties of this collective  
135 behavior and how it echoes the magnetic properties developed in free-living prokaryotes (*i.e.*, MTB). As  
136 long as magnetotaxis provides a selective advantage (20), the function is supposed to have been optimized  
137 over the time of holobiont diversification. If so, to what extent did holobionts converge toward the same  
138 motility behavior in response to chemical gradients and magnetic fields as in prokaryotes? And since cell  
139 polarity, flagella organization, magnetosomes arrangement, number and polarity impact magnetic behavior  
140 in free-living MTB (21–25), how are these features organized by symbionts to maintain a successful  
141 magnetic guidance at the scale of the consortium?

142

143           Here, we employ light-, electron- and X-ray-based microscopy techniques to characterize the  
144 motility, the ultrastructure and the magnetic properties of MHBs. The calculated magnetic dipole of MHBs  
145 from magnetic field-based motility assays was found to be more than two orders of magnitude greater than  
146 free-living MTB, an amount clearly in excess of that required to gain a magnetotactic advantage.  
147 Microscopy imaging of MHB ultrastructure (using scanning electron microscopy (SEM), transmission  
148 electron microscopy (TEM), scanning-TEM (STEM), cryo soft X-ray tomography (cryo-SXT)) and  
149 spectroscopic investigation of magnetosome magnetic properties (using X-ray magnetic circular dichroism  
150 (XMCD)) confirm a cohesive organization of ectosymbiotic cells and consistent magnetic dipole direction  
151 of magnetosome chains relative to the host, which confers an ultrasensitive magnetotaxis property to the  
152 holobiont. Lastly, unlike previously reported magnetite ( $\text{Fe}_3\text{O}_4$ ) crystal morphology in *Deltaproteobacteria*,  
153 we discovered that ectosymbiotic bacteria produce rhomboidal dodecahedron-like particles. From the  
154 microscale to the nanoscale, the results support hypotheses that the positioning, organization and number  
155 of ectosymbiotic cells and magnetosome chains are overly optimized by symbionts to insure a collective  
156 magnetotaxis similar to the magnetotaxis behavior observed in MTB. Furthermore, these results stimulate  
157 the debate of magnetosomes function beyond magnetotaxis since the additive magnetic moment is orders  
158 of magnitude in excess of that required for effective magnetotaxis.

159 **Results**

160 *Magnetotactic holobionts have a magnetotactic behavior similar to free-living magnetotactic bacteria*

161 Since the first description of magnetotactic holobionts (MHBs) (17), we have continuously collected  
162 samples in Carry-le-Rouet, France (Mediterranean Sea), to have a sufficient number of south-seeking  
163 MHBs to perform an extensive characterization of their ultrastructure and magnetotaxis. SEM and light  
164 microscopy observations show two thick flagella, each measuring about two to three times the length of the  
165 cell body, which is typical in Euglenids (Movie S1 and Fig. 1A). Transverse section of the flagella shows  
166 a canonical ‘9+2’ microtubule axoneme structure (Fig. S1) (26). SEM and TEM indicate that both flagella  
167 emerge from a large depression (Fig. 1) from the anterior pole where the protist is only partially covered  
168 by few magnetic ectosymbiotic bacteria (MEB) in contrast to the rest of its cell body (Fig. 1D and E). SEM  
169 observations at low electron energy show magnetic ectosymbiotic bacteria (MEB) densely cover the surface  
170 of the protist (Fig. 1B), while imaging at higher electron energy confirmed that they contained structurally-  
171 aligned nanoparticle chains (Fig. 1C).

172 We assessed the extent to which collective magnetotaxis evolved towards the same motility  
173 behavior as the one observed in single-celled MTB. Magnetic moments of MHBs were obtained by  
174 analyzing their U-turn motion (Fig. 2A and B present optical image of MHB in recorded video and  
175 schematic of U-turn experiment, Fig. S2 presents additional extracted motility parameters), which relates  
176 the radius and turning time of MHBs upon external magnetic field reversal using the following equation  
177 (27):

178 
$$\tau_{Uturn} = \frac{A}{M \cdot B} \cdot \ln \left( \frac{2 \cdot M \cdot B}{k_B T} \right) \quad (1)$$

179 Here,  $\tau_{Uturn}$  corresponds to the time the MHB take to make a U-turn upon switching the applied magnetic  
180 field ( $B$ );  $M$  is the magnetic moment of the MHB;  $k_B$  corresponds to the Boltzmann constant and  $T$  the  
181 temperature at which the experiment was performed (25°C).  $A$  is a constant related to a viscous torque. By  
182 considering the MHB shape to be an ellipsoid (17), it is defined as:

183 
$$A = \left(\frac{16}{3}\right)\pi\eta c^3 \cdot \left[\frac{1}{2} \cdot \ln \left(\frac{(a+c)}{(a-c)}\right) - \frac{(a \cdot c)}{b^2}\right] \quad (2)$$

184 Where  $\eta$  corresponds to the media viscosity (*i.e.*, Mediterranean Sea viscosity at 25 °C),  $a$  (10  $\mu\text{m}$ ) and  $b$   
185 (5  $\mu\text{m}$ ) are the major and minor axes of the ellipsoid, respectively, and  $c^2 = a^2 - b^2$ . The MHB U-turn  
186 time ( $\tau_{Uturn}$ ) was determined by tracking the U-turn trajectory and then plotting the first derivative,

187 corresponding to the instantaneous velocity (Fig. 2C), where the change in sign corresponds to the change  
188 in direction. Then, by taking the time difference between maximum and minimum peaks (shown in Fig.  
189 2D), the value of  $\tau$  is obtained and therefore  $M$  can be calculated from equation (1). A set of MHB U-turn  
190 trajectories ( $n = 22$ ) were tracked to calculate  $\tau_{\text{Uturn}}$  and  $M$ . We obtained an average absolute value of the  
191 magnetic moment  $M = 1.8 \pm 0.8 \times 10^{-13} \text{ A}\cdot\text{m}^2$ . Similar magnetic moments have been found for *Candidatus*  
192 *Magnetoglobus multicellularis* (between  $9 \pm 2 \times 10^{-15}$  and  $20 \pm 3 \times 10^{-15} \text{ A}\cdot\text{m}^2$  (28)) and magnetotactic  
193 protists ( $6.7 \times 10^{-12} \text{ A}\cdot\text{m}^2$  (29) and  $2.5 \pm 1.2 \times 10^{-13} \text{ A}\cdot\text{m}^2$  (30)). As a comparison, the magnetic moment of  
194 *Magnetospirillum gryphiswaldense* (MSR-1) was previously determined to be  $2.5 \pm 0.5 \times 10^{-16} \text{ A}\cdot\text{m}^2$  (31)  
195 or around  $7.7 \times 10^{-16} \text{ A}\cdot\text{m}^2$  by direct measurement of the magnetosome chain using magnetic tweezers (32).  
196 Similar magnetic moments have been found for other species of MTB as well (33, 34).

### 197 ***Ectosymbiotic cells are parallel to each other and oriented along the long axis of their protistan host***

198 To obtain a global understanding of MEB organization in their native-state configuration (*i.e.*, without  
199 congealing artifacts from fixation processes), MHB samples were vitrified for cryo soft X-ray tomography  
200 (cryo-SXT) imaging. Cryo-SXT offers a relatively deep penetration and enhanced natural contrast of  
201 biological materials in the water window (*i.e.*, X-ray absorption from C and N K-edges) without chemical  
202 fixation or staining. Fig. 3A presents tomogram reconstructed slices of the vitrified MHB captured with an  
203 incident energy of 520 eV (raw X-ray image of this MHB and tilt-series images are shown in Fig. S3, see  
204 Movie S2 for tomogram video). Owing to a voxel size of  $(12 \text{ nm})^3$  and the high density of magnetite  
205 nanocrystals, magnetosome chains were distinguishable in MEB from tomography virtual slices and were  
206 assigned during volume segmentation (see Materials and Methods). The segmentation of the entire volume  
207 reconstruction is presented in Fig. 3B with magnetosome chains in red, MEB membrane in yellow (only  
208 partially reconstructed due to limited contrast in the tomographic volume), protistan host in cyan (*i.e.*, outer  
209 membrane and intracellular compartments) and dense intracellular granules in white (identified as  
210 phosphorus- and calcium-rich granules using X-ray energy-dispersive spectrometry (XEDS); Fig. S4). The  
211 bottom side of the MHB (in contact with the carbon film of TEM grid) was flattened likely due to  
212 sedimentation or the vitrification process. This can be observed from the “front” and “side” views of the  
213 reconstructed model (Fig 3B, right panels). When considering the magnetosome chains in red; Fig. S5  
214 shows only this reconstructed volume and the protistan host. We note the magnetosome organization has a  
215 general similarity to that identified with multicellular magnetotactic prokaryotes (MMPs) (35, 36);  
216 magnetosomes are found at the exterior of the consortium and they align in the direction from pole to pole.  
217 For MMPs, however, magnetosomes organize into chain-like clusters, not distinct chains as for the MHB.

218 Thin-sections of MHB confirmed that the protistan host is covered by one layer of longitudinally  
219 arranged, curved rod-shaped ectosymbiotic bacteria (Fig. 1D and 4A and B). Bacterial cells are localized  
220 within an invagination of the outer membrane of their host (Fig. 4A-C). Such channel-like structures may  
221 help the bacteria to maintain position at the surface of the eukaryotic host and increase their surface contact  
222 with the host for increased transfer of material for chemical symbiosis-related exchanges. Transversal  
223 sections of ectosymbionts revealed a consistent and unique morphology (Fig. 4A-E). As previously reported  
224 (17), transversal sections indicate the presence of wing-like structures in all ectosymbionts. Here, we show  
225 that these structures are protrusions from the external membrane only (Fig. 4C-E) with one of the wing  
226 structures often below and the other above neighboring bacterial cells (Fig. 4D). These structures could also  
227 be observed from SEM images where they appear as tapered edges (Fig. S6). The linking of adjacent wing  
228 structures may help to improve ectosymbiotic cells cohesion. Longitudinal and transversal sections also  
229 reveal the presence of vesicles (*i.e.*, round structures) between bacteria that could also be involved in the  
230 fixation of the symbionts (Fig. 4c-f). These vesicles could also be part of the communication between MEB  
231 to coordinate their activities such as cell division. Similar to the vesicles previously observed in MMPs  
232 (21). The presence of the ectosymbiotic bacteria in the vicinity of hydrogenosomes produced by the protist  
233 was also confirmed (Fig. 4C and D).

234 Transversal sections indicate that magnetosomes are always positioned in the lower half of the  
235 MEB cell body, closer to the host (Fig. 4A-E) or on side of the MEB with shorter inner curvature radius.  
236 Similar magnetosome positioning at midcell was previously reported in the free-living *Magnetospirillum*  
237 *gryphiswaldense* MSR-1. It was shown that the cytoskeletal determinant CcfM links the magnetoskeleton  
238 (*i.e.*, magnetosome-specific cytoskeleton produced by specific proteins such as MamK) to cell morphology  
239 in regions of inner positive-cell curvature (22). In the case of MEB, such positioning of the magnetosome  
240 chain could represent an advantage for optimizing the magnetic moment of the MHB. Although the genome  
241 of MEB did not contain any orthologue of CcfM, it is possible that another molecular pathway is involved  
242 in magnetosome positioning in MHBs.

243 All magnetosome chains are aligned along the long axis of the host cell. Towards the front or back  
244 of the host, magnetosome chains are tilted inward (*i.e.*, following the curvature of the host cell), indicating  
245 a close contact between MEB and the surface of the host cell. From cryo-SXT volume reconstruction (Fig.  
246 3) and TEM thin sections (Fig. 4), parallel magnetosome chains are typically spaced 0.5-1  $\mu\text{m}$  apart.  
247 Considering the potential for interchain interactions to influence the ensemble magnetic properties,  
248 micromagnetic calculations of simulated magnetosome chain structures were conducted using MERRILL  
249 (v1.6.4) (see Materials and Methods) (37). Based on the average particle size, spacing and number of  
250 particles per chain as measured by TEM, a chain of 25 rhomboidal dodecahedral nanocrystals (see section

251 below for the characterization of the nanocrystal shape) with a mid-sphere diameter of 60 nm and 10 nm  
252 spacing between grains was built to model the adjacent stray fields. Based on this calculation (Fig. S7),  
253 stray fields at least 1  $\mu\text{m}$  from the chain (in both parallel and perpendicular directions) are consistently more  
254 than three orders of magnitude weaker than the remnant magnetization ( $M_{\text{rs}}$ ) of the entire chain ( $8.4 \times 10^{-16}$   
255  $\text{A}\cdot\text{m}^2$ , see Materials and Methods), ruling out significant interchain interactions. Moreover, the magnetic  
256 moment for one of the modelled magnetosome chain structures is high enough to overcome Brownian  
257 motion at 20 °C in a magnetic field of 10  $\mu\text{T}$ . To impart a magnetotactic advantage for MHBs over other  
258 microorganisms of similar size (*i.e.*, a net average bias (> 50 % of the population) of  $n$  cells aligned with  
259 the magnetic field direction against randomized orientation caused by Brownian motion), we considered  
260 how the magnetic moment of magnetosome chains decrease because of their bending to follow curvature  
261 of the host cell (Fig. S8). Regardless of these few chains at the extreme ends of the cell, which are highly  
262 curved, we estimate that net cell magnetization from only a few chains positioned close to the middle section  
263 of the host is sufficient to confer magnetotaxis on the MHB (see Fig. S8 and Materials and Methods). The  
264 total magnetic moment of the holobiont being  $1.8 \times 10^{-13} \text{A}\cdot\text{m}^2$  and that of a single magnetosome chain  $8.4$   
265  $\times 10^{-16} \text{A}\cdot\text{m}^2$ , with most of the magnetosome chains aligned parallel to each other, our model would indicate  
266 there are about 215 chains attached to the host which is consistent with microscopy observation (100-200  
267 MEB/holobiont) (17).

### 268 ***Magnetic moments of magnetosome chains align to enhance magnetotaxis ability of their host***

269 Considering magnetosome chain organization, negligible interchain interaction, and the above-calculated  
270 ensemble magnetic moment of MHBs, the magnetic moment of each chain should contribute independently  
271 and additively to the magnetic moment the host cell experiences. This assumption was tested by measuring  
272 the native-state magnetic moment of individual chains *via* scanning transmission X-ray microscopy with  
273 X-ray magnetic circular dichroism (STXM-XMCD) in the absence of applied magnetic fields.

274 For STXM-XMCD sample preparation, MHB samples were magnetically extracted from  
275 environmental samples using weak magnetic fields (see Materials and Methods). Further, when collecting  
276 XMCD, no magnetic fields were applied on the sample. Instead, the sample was tilted  $\sim 30^\circ$  to the normal  
277 plane to probe the intrinsic magnetization of each magnetite nanocrystal (Fig. S9A and B for experimental  
278 setup) (38). MHBs with magnetosome chains positioned perpendicular to the axis of rotation of the sample  
279 holder were analyzed to optimize the XMCD signal. This is because the magnetization easy axis is typically  
280 aligned along the magnetosome chain direction, *i.e.*,  $\langle 111 \rangle$  crystallographic direction of magnetite (see  
281 below for high-resolution TEM analyses; (39–41)). Furthermore, it was important to identify MHBs that

282 had intact flagella, so that a correlation between the magnetization of magnetosome chains and the  
283 swimming direction (*i.e.*, south-seeking) could be assessed.

284 Fig. 5A and B present STXM images of two different MHBs positioned in opposite directions and  
285 observed at 710 eV (*i.e.*, at the Fe L<sub>3</sub>-edge), where magnetosome chains are most visible against the host  
286 cell. At this energy, it is also possible to observe the flagella of the deposited MHBs (confirmed with optical  
287 microscopy). We then utilized three energy points in the Fe L<sub>3</sub>-edge absorption region that show the  
288 maximum XMCD response (708.8, 709.8 and 710.7 eV, see Fig. S9C for identification of these energies)  
289 to collect maps with both circular polarizations of incident X-rays (circular polarized left (CPL) and right  
290 (CPR)). Higher resolution analyses on regions of interest for the first MHB show differences in signal  
291 intensity between circular polarizations (Fig. 5C). Based on the tilt direction of the sample holder, the  
292 orientation of MHB (*i.e.*, swimming direction) and the circular polarization, the resulting color in the  
293 XMCD difference maps indicates the direction of magnetization. Here, the red color indicates  
294 magnetization in the right direction (Fig. 5C), while blue indicates magnetization in the left direction (Fig.  
295 5D). As seen from the presented XMCD difference maps, the projected magnetization of magnetosome  
296 chains is mostly uniform, pointing towards the flagella end of the MHB. This was confirmed by measuring  
297 another MHB with the flagella on the opposite side (Fig. 5B and D). In total, three MHB were analyzed  
298 (Fig. S10 shows the third MHB without chemical fixation), consistently demonstrating magnetic dipoles of  
299 magnetosome chains are in the same direction among ectosymbionts with their magnetic south pole  
300 pointing toward the flagella, thus optimizing the swimming direction of the protistan host toward the south.  
301 This suggests magnetic dipole direction is maintained for dividing ectosymbionts. A similar conservation  
302 of magnetic dipole direction relative to consortium structure during division has also been identified for  
303 multicellular magnetotactic prokaryotes (MMPs) (42).

304 An inversion of individual magnetic dipole direction against the overall magnetization vector was  
305 discovered on a few occasions, which occurs in the middle or at the end of magnetosome chains. These  
306 inversions are evident by the alternating red-blue regions in the CPL-CPR difference maps (Fig. 5C). These  
307 inversions also confirm the magnetic field strength used to extract MHBs from collected sediment did not  
308 disturb native magnetic moments of magnetosomes. The crystalline orientation of magnetosome particles  
309 in one inversion region was revisited and examined using scanning transmission electron microscopy high-  
310 angle annular dark field (STEM-HAADF) imaging. Fig. S11 shows the STXM region in Fig. 5A (top left  
311 region, purple frame) and plots the  $\langle 111 \rangle$  alignment of individual particles as found from FFT and  
312 stereographic projections. This demonstrates the consistent alignment of magnetite's easy axis  $\langle 111 \rangle$  with  
313 the chain direction despite the inversion of magnetic dipoles.

314 We then performed further HR-TEM analyses of individual magnetosomes for three MEB from  
315 three different MHBs, confirming expected {111}, {100} and {110} faces of magnetite nanocrystals (Fig.  
316 6) and identifying the nanocrystal orientation in chain structures. The <111> crystallographic direction of  
317 each particle was almost systematically aligned along the chain length. This is consistent with the  
318 orientation generally observed for individual MTB biomineralizing prismatic magnetite (41). Upon close  
319 inspection of several individual magnetosomes, the shape of most magnetite nanocrystals is best described  
320 as a rhomboidal dodecahedron (Fig. S12 and S13), a morphology that exhibits only {110} faces. Fig. S14  
321 and S15 present additional HR-TEM analyses of individual particles and demonstrate the consistent <111>  
322 alignment with chain direction and further this unexpected nanocrystal shape for magnetite. This  
323 crystallographic form of magnetite from a magnetosome-producing bacterium of the *Deltaproteobacteria*  
324 class is unanticipated, which suggests previous studies that correlated the nanocrystal morphology formed  
325 by a bacterium and its phylogenetic position should be reconsidered (41, 43, 44).

326

## 327 **Discussion**

328 Many microorganisms, including bacteria, microeukaryotes and archaea, live together permanently or at  
329 least transitorily by forming microbial holobionts. These intimate relationships must not only satisfy  
330 metabolic requirements, but their physical assembly must maintain, and even improve, holobiont integrity  
331 and motion. This study utilized a suite of imaging and characterization tools to generate insights on one of  
332 the most fundamental cases of collective magnetotaxis known, ranging from motility in magnetic fields,  
333 three-dimensional organization of magnetosome chains around the host cell, polarity of magnetic dipoles,  
334 ultrastructure of bacterial cells at the surface of the host, down to the morphology of magnetite nanocrystals.  
335 Based on the different scales of our analysis, the MHB studied here is a model system apt to be investigated  
336 with the electron and X-ray based imaging, which provide the adequate spatial resolutions to capture the  
337 intricate organization at both cellular and nanoparticle size regimes. Based on MHBs, what can symbiosis  
338 research gain from such collective motion and physical characterization studies?

339 The first finding is that a similar field-guided motility has emerged independently in free-living  
340 single-celled MTB and in microeukaryotes through symbioses, although the magnetosome organelle has a  
341 common prokaryotic origin. The magnetic moment determined using U-turn analysis was  $1.8 \pm 0.8 \times 10^{-13}$   
342  $\text{A}\cdot\text{m}^2$  ( $n = 22$ ), a value more than two orders of magnitude higher than the magnetic moment of a single  
343 MTB (45–49). This magnitude of magnetic interaction with the geomagnetic field is in excess for the MHB.  
344 Our micromagnetic calculations on the magnetic dipole strength of simulated magnetosome chains and the

345 size and shape of the entire holobiont estimate (considering Brownian motion at 20 °C) that only a few  
346 magnetosome chains – not dozens – positioned longitudinally along the mid-section of the host cell would  
347 be sufficient for the protist cell to gain a magnetotactic advantage (in fields > 10  $\mu$ T) over other motile  
348 microorganisms of similar size (see Fig. S8 and Materials and Methods). It was then hypothesized from  
349 this calculation and our characterization of the MHB that perhaps more magnetosome chains were  
350 necessary during periods of weak geomagnetic field strength in Earth’s history. However, even with a field  
351 strength of  $\sim$ 1  $\mu$ T, only a few additional magnetosome chains contributing to the additive magnetic moment  
352 of a holobiont would be required (Fig. S8). Therefore, the dozens of magnetosome chains that cover the  
353 MHB are greatly in excess of what is required for effective magnetotaxis. Similar observations have been  
354 made in the magnetotactic multicellular prokaryotes where their magnetic moment was optimized to a large  
355 degree (28, 36, 42).

356 At the magnetosome level, we observed a uniformity of magnetic dipole direction in MEB.  
357 However, as presented in Fig. 5C, inversion of magnetosome magnetic dipole was detected on a few  
358 occasions, although its origin could not be determined by the present work. We note that magnetic dipole  
359 inversions have been reported for MTB strains MV-1 and AMB-1 when a similar XMCD-STXM  
360 measurement was performed (38, 50). In the case of *Magnetospirillum magneticum* (AMB-1) studies,  
361 inversion of an entire magnetosome chain segment was found for a mature cell, whereas out-of-plane  
362 magnetic dipoles were found for recently biomineralized magnetosomes. For MHB, the alternating  
363 inversions of individual magnetosomes do not appear to originate from immature magnetosomes as these  
364 particles are found mid chain, spaced closely to other magnetosomes, and are of average particle size.  
365 Regardless of this irregularity to be further understood, the consistent alignment of chain magnetic dipoles  
366 is an indicator of highly controlled cell division (24) and appropriation of chains on the host cell to maintain  
367 the maximum magnetic moment. This is in contrast to a recent finding by Leão *et al.* (30) where bundles  
368 or clusters of bullet-shaped magnetosomes were discovered in a flagellated protist that showed a seemingly  
369 random organization of magnetosome magnetic dipoles.

370 TEM examinations reveal additional interesting features: bionts have evolved specific structures  
371 and three-dimensional organization to optimize holobiont stability and hydrodynamics. Chains and MEB  
372 cells are parallel to the microeukaryote/holobiont motility axis, and extracellular vesicles and MEB wing-  
373 like protrusions seem to stick and arrange bionts together in this orientation. This reveals that beyond the  
374 chemical symbiosis previously described between host and ectosymbiotic bacteria (17), the holobiont  
375 collective behavior emerges from physical interactions between biological interfaces (positioning and  
376 structural integrity of ectosymbiotic bacteria on the host) and between magnetic dipoles and the  
377 geomagnetic field (retention of magnetic dipole direction with respect to direction of motility). These

378 physical constraints may act on biology to drive the adaptive evolution of the holobiont. Without complying  
379 to these physical restrictions, the consortium's persistence would be challenged.

380         Such a biological constraint exerted by magnetotaxis suggests an important ecological role for the  
381 holobiont. As hypothesized previously (17), the host benefits from the same advantages as MTB in chemical  
382 gradients, namely, finding more easily optimal chemical redox conditions in fluctuating environments.  
383 Collective magnetotaxis may thus optimize holobiont efficiency for nutrient acquisition or avoidance of  
384 toxic substances. Sharing the function with the protistan host may avoid the metabolic burden of  
385 synthesizing flagellar components for MEB, the energetic expense of fueling flagellar motors and the  
386 exposure of some molecules that could be recognized by predators. More environmental and genomic data  
387 will resolve the adaptive history, but can the biophysical characterization of MHBs give insights into the  
388 syntrophy itself or the fundamental role of magnetosomes in MTB? Attention has been paid to the  
389 geolocation function of magnetosomes to explain the emergence of such a biomineral and organelle (43,  
390 51, 52). However, if this primary function requires only few magnetosome chains in MHBs, then why is  
391 the magnitude of magnetic interaction with the geomagnetic field excessive, and why do MEB continue to  
392 spend energy to produce such an excess number of magnetosomes? Here, MHBs provide further evidence  
393 that magnetosomes might also be involved in metabolic aspects and possibly syntrophy. Similar to what  
394 has been proposed for MTB, MEB could act as a battery to fuel the protist (53). The close vicinity of  
395 magnetosomes to the protist's external membrane could evidence a possible traffic of energy from  
396 prokaryotic cells toward the eukaryotic host, similar to how hydrogenosomes function but in the opposite  
397 direction (*i.e.*, fueling the MEB with H<sub>2</sub>) (17, 54). Another hypothesis explaining such a large amount of  
398 magnetosomes in MHBs is an antioxidant defense. Indeed, it was shown in model MTB strains of the  
399 *Magnetospirillum* genus that magnetosomes exhibit a peroxidase-like activity (55, 56). Magnetosomes  
400 were proposed to decrease and eliminate reactive oxygen species (ROS) in the cell. Thus, in MHBs,  
401 ectosymbiotic cells could serve as a sink for the ROS produced by their protistan host during metabolic  
402 activity or exposure to oxygen (57). Although little is known about the physiology of this MHB protist and  
403 its closest relatives, it is possible that they require a high concentration of iron for metabolic needs. Since  
404 MTB are known to be very efficient in the uptake of iron (58), the protist could benefit from the iron uptake  
405 by its symbionts with the transfer of iron from the ectosymbionts toward the protist.

406         Magnetotaxis in MTB is usually described as a passive orientation and active swimming along the  
407 Earth's magnetic field lines thanks to magnetosomes and to flagella, respectively (59). However, it was  
408 shown that a potential magnetic sensing, *via* the widely used chemotaxis mechanism, might be actively  
409 involved in magnetotaxis (60). In *Magnetospirillum magneticum* AMB-1, a methyl-accepting chemotaxis  
410 protein (MCP) appears to interact with the protein MamK involved in magnetosome chain formation. This  
411 finding led to the hypothesis that the magnetic torque applied on the magnetosome chain might be relayed

412 by MamK and transferred to MCPs at the cell poles *via* specific interactions between them. The chemotaxis  
413 signal transduction system may then take over the subsequent response of the cell. In MHBs, it is likely  
414 that such signal transduction system between the MEB magnetosome chains and the host flagellar motor is  
415 absent as it was shown that none of the genes encoding classical chemotaxis pathways were detected in the  
416 genome of MEB (17). Thus, to overcome potential swimming deviation against the Earth's magnetic field,  
417 a last hypothesis to consider is that the higher the number of magnetosome chains, the better MHBs can  
418 maintain a swimming direction parallel to the magnetic field.

419 Future studies that inspect MHBs under laboratory-based conditions and their diversity in aquatic  
420 environments will hopefully reveal more on the function of magnetosomes for eukaryotes. The discovery  
421 of collective magnetotaxis has opened up a new interdisciplinary field of study in biology and biophysics  
422 to answer the questions this symbiosis between eukaryotes and prokaryotes generates on their evolution  
423 (*i.e.*, were ectosymbiotic bacteria originally recruited with the ability to produce magnetosomes or was the  
424 formation of magnetosomes acquired by the bacteria after they started their symbiosis with their host?) and  
425 functioning (*i.e.*, what major advantages does the protist obtain by carrying dozens of biomineralizing  
426 bacteria on its surface?).

427

## 428 **Materials and Methods**

429 **Sample collection and light microscopy observations.** Samples were collected by free-diving at a water  
430 depth of 0.5-2 m in the Mediterranean Sea, in Carry-le-Rouet (43.334222°N, 5.175278°E). One-liter glass  
431 bottles were filled to about 0.3-0.5 of their volume with sediment, then filled to their capacity with water  
432 that overlaid the sediment. Air bubbles were excluded. Once in the laboratory, samples were stored under  
433 dim light at room temperature (~ 25 °C). South-seeking magnetotactic holobionts were concentrated by  
434 placing a magnetic stirring bar (~ 10 mT) next to the bottles, above the sediment-water interface for 2 h.  
435 Examination of magnetically concentrated cells was carried out using the hanging drop technique (61)  
436 under a Zeiss Primo Star light microscope equipped with phase-contrast and differential interference  
437 contrast optics. The local magnetic field used to determine magnetotaxis was reversed by rotating the  
438 stirring bar magnet 180 ° on the microscope stage.

439 **Movement and magnetotactic response analysis.** A customized magnetic microscope equipped with a  
440 triaxial Helmholtz coilset and controller (C-SpinCoil-XYZ, Micro Magnetics Inc.) and a Andor Zyla 5.5  
441 high speed camera was used (62). The 3D-axis Helmholtz coils can generate DC magnetic fields with a  
442 precision of 5 % of Earth's magnetic field ( $\pm 2.5 \mu\text{T}$ ). Using the setup, we programmed the switching of

443 the magnetic field between -3.5 and +3.5 mT for the U-turn. For U-turn measurements, the magnetic field  
444 was fixed for 2 s before switching. The switching was repeated to collect at least three U-turns in the field  
445 of view. The trajectories and U-turn of 22 MHB were extracted and smoothed by a tracking script written  
446 in python and based on the OpenCV Object Tracking Algorithms with the CSRT tracker. The data is  
447 smoothed by a convolution-based smoothing approach. For both trajectory and U-turn measurements, a  
448 20X objective (N.A. 0.45) was used. The mathematical relation to calculate the MHB magnetic moment  
449 from the U-turn time are described in the main text by equations (1) and (2). The fsolve function from  
450 Octave/Matlab was used to obtain  $M$  from equation (1). Data fitting was done by the intrinsic fitting  
451 functions of OriginPro, Version 2016 (OriginLab Corporation, Northampton, MA, USA).

452 **Scanning electron microscopy (SEM).** Magnetically concentrated MHB were fixed in a solution of 1 %  
453 paraformaldehyde and deposited on a glass coverslip coated with poly-L-lysine and stored at 4 °C. Before  
454 the observation, the sample was dehydrated in successive ethanol baths (50 %, 70 %, 96 %, 100 %) then  
455 processed through critical point drying (CPD) (Leica EM CPD300) before coating with carbon (Leica EM  
456 SCD500). Images were collected in the backscattered and secondary electron modes using a Zeiss Ultra 55  
457 FEG-SEM operating at 1–10 kV, a working distance of 4 mm and an aperture of 10–60  $\mu\text{m}$ .

458 **Transmission electron microscopes (TEM).** TEM was used on ultrathin sections to characterize the  
459 ultrastructure of the magnetotactic holobionts. Thin-sectioned samples were prepared from magnetically  
460 concentrated protists fixed in 2.5 % (w/v) glutaraldehyde in sodium cacodylate buffer (0.1 M, pH 7.4) and  
461 kept at 4 °C for at least 24 h. Due to the low biomass of MHB, fixed cells were embedded in a small agarose  
462 plug to facilitate their transfer in the different solutions before the inclusion in resin. Cells were post-fixed  
463 one hour with 1 % (w/v) of osmium tetroxide. Cells were then dehydrated with successive ethanol baths  
464 (30, 50 70, 90, 100 %) with increasing concentrations and finally embedded in the resin (Epon 812).  
465 Sections (40 nm thick and 3 mm long) were cut with the UC7RT ultramicrotome (Leica Microsystems  
466 GmbH), deposited onto TEM copper grids and stained with uranylless solution for 10 min and Reynolds  
467 lead citrate 3% for 3 min. Electron micrographs were recorded with a Tecnai G2 BioTWIN (FEI Company,  
468 Eindhoven, Netherlands) equipped with a CCD camera (Megaview III, Olympus Soft imaging Solutions  
469 GmbH, Münster, Germany) with an accelerating voltage of 100 kV. The sizes of magnetosomes were  
470 measured from TEM images using the ImageJ software (v1.48).

471 **High-resolution transmission electron microscopes (HRTEM) and X-ray energy-dispersive**  
472 **spectrometry (XEDS).** HRTEM was performed on cells directly deposited onto TEM copper grids coated  
473 with a carbon film. HRTEM and z-contrast imaging in the high-angle annular dark field (STEM-HAADF)  
474 mode, and elemental mapping by XEDS were carried out using a JEOL 2100 F microscope operating at

475 200 kV. This machine was equipped with a Schottky emission gun and an ultra-high-resolution pole piece.  
476 HRTEM images were obtained with a Gatan US 4000 charge-coupled-device (CCD) camera.

477 **Cryo soft X-ray tomography (cryo-SXT).** Imaging was conducted at ALBA synchrotron using cryo  
478 transmission X-ray microscopy at Mistral beamline (Barcelona, Spain) (63) under the awarded proposals  
479 2018022677 and 2019023346. Using a similar approach to that described above, MHB samples were  
480 magnetically concentrated on the wall of an environmental sample bottle and then extracted by  
481 micropipette. 5  $\mu$ L of the magnetically concentrated MHB extract along with 1  $\mu$ L of 100 nm Au  
482 nanoparticles (BBI Solutions concentrated 5X) were added to a poly-l-lysine coated transmission electron  
483 microscopy grids (Quantafoil R2/2 holey carbon, gold). Gold nanoparticles of 100 nm deposited on the grid  
484 served as fiducial markers for projection alignment prior to tomographic reconstruction. The grid was  
485 incubated horizontally for 1-2 min to allow deposition of MHB on the grid. The grid was then vertically  
486 loaded into a Leica EM GP plunge freezer at 95 % humidity, blotted from the back of the grid with filter  
487 paper (3 s blotting time) and then quickly dropped into a liquid ethane container (-180 °C) cooled by liquid  
488 nitrogen. Vitrified cells were kept under cryogenic conditions until being transferred to the MISTRAL  
489 beamline cryo chamber for measurement. Tomograms of two MHB were collected.

490 A tilt series of projections from -65 ° to +65 ° was collected every 1 ° with an incident X-ray energy  
491 of 520 eV. Exposure time varied from 1-2 s for each projection (2 s at higher angles). The sample was  
492 imaged at 0 ° before and after collecting the tilt series to ensure there was no significant beam damage at  
493 the achievable resolution. A 40 nm Fresnel zone plate was used with an effective pixel size of 12 nm. The  
494 projections were normalized with the incoming flux and deconvolved with the measured point spread  
495 function (PSF) of the optical system (64). Alignment of projections was done with Etomo using Au fiducials  
496 of 100 nm. Tomographic reconstruction and SIRT deconvolution were performed using IMOD. Volume  
497 segmentation and visualization of tomograms was conducted using Microscopy Image Browser (65) and  
498 Amira (FEI, USA) (66). Although this approach conserves the organization of MHB cells in their native-  
499 state configuration, partial detachment of ectosymbionts was observed. However, the majority of bacteria  
500 and their overall organization at the surface of their host were maintained.

501 **Scanning transmission X-ray microscopy (STXM) and X-ray magnetic circular dichroism (XMCD).**  
502 Magnetotactic holobionts were magnetically concentrated using a low intensity magnet (~10 mT) for a  
503 maximum time of 30 min to avoid remagnetization or any magnetic disturbance/interference with  
504 magnetosomes. Cells were then transferred onto a light microscopy slide and magnetically transferred in a  
505 clean drop of filtered environmental seawater. Cells aggregated at the edge of the filtered drop were then  
506 micromanipulated with an InjectMan® NI2 micromanipulator and a CellTram® vario, hydraulic, manual

507 microinjector from Eppendorf mounted to a Leica DM IL LED microscope and further transferred in a drop  
508 of fixative buffer containing 2.5 % (w/v) glutaraldehyde in sodium cacodylate buffer (0.1 M, pH 7.4)  
509 prepared in filtered environmental seawater. Fixation occurred for only 10 seconds at room temperature  
510 before the transfer of the cells, using the micromanipulator, onto a TEM copper grid coated with a carbon  
511 film. A quick fixation was sufficient to conserve the ultrastructure of the holobiont and allow observation  
512 of the biont's magnetosomes in the TEM. After their preparation, TEM grids were observed with STXM  
513 without previous TEM analysis to avoid magnetic disturbance.

514 STXM-XMCD measurements were performed at HERMES, the soft X-ray spectromicroscopy  
515 beamline at SOLEIL synchrotron (St. Aubin, France) (67, 68). A 25 nm Fresnel zone plate was employed  
516 with measurements conducted under vacuum conditions at room temperature. Most STXM maps of MHB  
517 were collected at 710 eV (at the Fe  $L_3$ -edge). Circularly polarized right (CPR) and left (CPL) light was used  
518 without applied magnetic field to conserve the native-state magnetic moment of magnetosomes. To retrieve  
519 an XMCD signal without applied fields, the sample was tilted  $30^\circ$  relative to the focal plane to measure  
520 the intrinsic magnetic dipole moments of magnetosomes (38). XMCD maps were then generated from the  
521 difference of OD-converted CPR and CPL images at 708.8 eV, the energy at which the strongest XMCD  
522 signal was found. Other energies corresponded to 709.9 and 711.0 eV. Axis2000 and IgorPro software were  
523 used to perform image work-up, analyses and create XMCD maps. XMCD maps were obtained for at least  
524 five MEB of each of the three MHB measured.

525 **Micromagnetic simulations and calculations.** To determine the decay of the stray field from a straight  
526 chain of 25 magnetosomes, we use a non-interacting point dipole approximation. Each point dipole is taken  
527 to represent the center of a rhomboidal dodecahedron magnetosome with mid-sphere diameter of 60 nm  
528 (volume of  $7.0 \times 10^{-23} \text{ m}^3$ ), which, with a magnetite saturation magnetization of  $4.8 \times 10^5 \text{ A}\cdot\text{m}^{-1}$ , equates to  
529 a uniformly magnetized magnetosome moment of  $3.36 \times 10^{-17} \text{ A}\cdot\text{m}^2$  (total chain moment of  $8.40 \times 10^{-16}$   
530  $\text{A}\cdot\text{m}^2$ ;  $0.84 \text{ fA}\cdot\text{m}^2$ ). The magnetosome neighbor-to-neighbor edge separation is taken to be 10 nm. The net  
531 stray field is calculated as the sum of 25 magnetosome dipole fields at given distances parallel and  
532 perpendicular to the chain axis (Fig. S7).

533 Micromagnetic models were used to determine the effect of curved chains around the host cell.  
534 Magnetosome size, shape, and neighbor-to-neighbor edge separation are the same as described above. The  
535 magnetosome chains were arranged in an arc defined by a circle of a specified radius, while maintaining  
536 the face centered neighbor-to-neighbor edge separation of 10 nm. Mesh inputs were generated using Trelis  
537 v17.1. The micromagnetic calculations were performed using MERRILL v1.6.4 (37). An example of a  
538 micromagnetic solution is shown in Fig. S8.

539 For a population of cells, the average alignment,  $\langle \cos \theta \rangle$ , is dependent on the balance of magnetic  
540 energy rotating the cell towards the magnetic field and thermal energy of randomizing Brownian rotation.  
541 This can be expressed as:

$$542 \quad \langle \cos \theta \rangle = L\left(\frac{mB}{k_B T}\right)$$

543 where  $m$  is the net moment of each cell,  $B$  is the magnetic field intensity,  $T$  is the temperature,  $k_B$  is the  
544 Boltzmann constant, and  $L(x) = \coth x - 1/x$ , is the Langevin function. A magnetotactic advantage will  
545 be conferred to a population of cells if there is a net average bias of alignment of cells towards the magnetic  
546 field direction where  $\langle \cos \theta \rangle \geq 0.5$ . Over the past 10,000 years in the Mediterranean region, the field  
547 strength is consistently above 30  $\mu\text{T}$ , which, at 20  $^\circ\text{C}$ , equates to a minimum moment per cell of 0.24  $\text{fA}\cdot\text{m}^2$ .  
548 For an extremely weak field of 3  $\mu\text{T}$ , a minimum moment per cell of 2.4  $\text{fA}\cdot\text{m}^2$  is required to overcome  
549 Brownian motion and can be achieved with as few as two chains of magnetosomes (Fig. S8).

550

## 551 Acknowledgements

552 This work was supported by a grant from the CNRS – mission pour les initiatives transverses et  
553 interdisciplinaires (MITI), adaptation du vivant à son environnement, projet *SymbioAdapt* and a project  
554 from the French National Research Agency (ANR SymbioMagnet-21-CE02-0034-01). Romain Bolzoni  
555 PhD contract was supported by the CNRS – MITI. D.M.C. acknowledges research funding through a  
556 European Union Marie-Skłodowska Curie Action International Fellowship (MSCA-IF Project 797431:  
557 BioNanoMagnets). D.M.C. and D.F. acknowledge awarded ALBA synchrotron beamtimes (Proposals  
558 2018022677 and 2019023346), Mistral beamline staff for assistance in cryo-SXT experiments and  
559 CALIPSO funding for Proposal 2019023346. We acknowledge Soleil Synchrotron for beamtime awarded  
560 (Proposal 20191124) for experiments on the Hermes beamline (STXM-XMCD). W.W. would like to  
561 acknowledge support from the Natural Environmental Research Council (NERC) through grants  
562 NE/V001233/1 and NE/S011978/1. We thank Suri for his help in ultrathin-sections preparation. We thank  
563 Jean-Michel Guigner for managing the TEM facility at IMPMC. G.A.P. is funded by a Natural Environment  
564 Research Council Independent Research Fellowship (NE/P017266/1).

565

## 566 References

- 567 1. J.-B. Raina, *et al.*, Symbiosis in the microbial world: from ecology to genome evolution. *Biol. Open*  
568 7, bio032524 (2018).

- 569 2. L. Margulis, R. Fester, *Symbiosis as a Source of Evolutionary Innovation: Speciation and*  
570 *Morphogenesis* (MIT Press, 1991).
- 571 3. P. Lopez-Garcia, D. Moreira, The Syntrophy hypothesis for the origin of eukaryotes revisited. *Nat.*  
572 *Microbiol.* **5**, 655–667 (2020).
- 573 4. P. López-García, L. Eme, D. Moreira, Symbiosis in eukaryotic evolution. *J. Theor. Biol.* **434**, 20–33  
574 (2017).
- 575 5. P. Engel, N. A. Moran, The gut microbiota of insects - diversity in structure and function. *Fems*  
576 *Microbiol. Rev.* **37**, 699–735 (2013).
- 577 6. P. Vandenkoornhuys, A. Quaiser, M. Duhamel, A. Le Van, A. Dufresne, The importance of the  
578 microbiome of the plant holobiont. *New Phytol.* **206**, 1196–1206 (2015).
- 579 7. T. Woyke, *et al.*, Symbiosis insights through metagenomic analysis of a microbial consortium.  
580 *Nature* **443**, 950–955 (2006).
- 581 8. C. E. Harper, C. J. Hernandez, Cell biomechanics and mechanobiology in bacteria: Challenges and  
582 opportunities. *APL Bioeng.* **4**, 021501 (2020).
- 583 9. J. Decelle, *et al.*, Subcellular architecture and metabolic connection in the planktonic  
584 photosymbiosis between Collodaria (radiolarians) and their microalgae. *Environ. Microbiol.* **23**,  
585 6569–6586 (2021).
- 586 10. J.-C. Simon, J. R. Marchesi, C. Mougél, M.-A. Selosse, Host-microbiota interactions: from  
587 holobiont theory to analysis. *Microbiome* **7**, 5 (2019).
- 588 11. D. Faure, J.-C. Simon, T. Heulin, Holobiont: a conceptual framework to explore the eco-  
589 evolutionary and functional implications of host-microbiota interactions in all ecosystems. *New*  
590 *Phytol.* **218**, 1321–1324 (2018).
- 591 12. P. López-García, D. Moreira, Open questions on the origin of eukaryotes. *Trends Ecol. Evol.* **30**,  
592 697–708 (2015).
- 593 13. M. Müller, *et al.*, Biochemistry and evolution of anaerobic energy metabolism in eukaryotes.  
594 *Microbiol. Mol. Biol. Rev. MMBR* **76**, 444–495 (2012).
- 595 14. E. Hamann, *et al.*, Environmental Breviatea harbor mutualistic Arcobacter epibionts. *Nature* **534**,  
596 254–258 (2016).
- 597 15. T. Vicsek, A. Zafeiris, Collective motion. *Phys. Rep.* **517**, 71–140 (2012).
- 598 16. A. M. Wier, *et al.*, Spirochete attachment ultrastructure: Implications for the origin and evolution of  
599 cilia. *Biol. Bull.* **218**, 25–35 (2010).
- 600 17. C. L. Monteil, *et al.*, A symbiotic origin of magnetoreception in unicellular eukaryotes. *Nat.*  
601 *Microbiol.* **4**, 1088–1095 (2019).
- 602 18. D. A. Bazylinski, R. B. Frankel, Magnetosome formation in prokaryotes. *Nat. Rev. Microbiol.* **2**,  
603 217–230 (2004).

- 604 19. C. T. Lefèvre, *et al.*, Diversity of magneto-aerotactic behaviors and oxygen sensing mechanisms in  
605 cultured magnetotactic bacteria. *Biophys. J.* **107**, 527–538 (2014).
- 606 20. X. Mao, R. Egli, X. Liu, L. Zhao, Magnetotactic advantage in stable sediment by long-term  
607 observations of magnetotactic bacteria in Earth’s field, zero field and alternating field. *PLoS One* **17**,  
608 e0263593 (2022).
- 609 21. X.-X. Qian, *et al.*, Juxtaposed membranes underpin cellular adhesion and display unilateral cell  
610 division of multicellular magnetotactic prokaryotes. *Environ. Microbiol.* **22**, 1481–1494 (2020).
- 611 22. D. Pfeiffer, *et al.*, A bacterial cytolinker couples positioning of magnetic organelles to cell shape  
612 control. *Proc. Natl. Acad. Sci. U. S. A.* **117**, 32086–32097 (2020).
- 613 23. M. Toro-Nahuelpan, *et al.*, MamY is a membrane-bound protein that aligns magnetosomes and the  
614 motility axis of helical magnetotactic bacteria. *Nat. Microbiol.* **4**, 1978–1989 (2019).
- 615 24. C. T. Lefèvre, M. Bennet, S. Klumpp, D. Faivre, Positioning the Flagellum at the Center of a  
616 Dividing Cell To Combine Bacterial Division with Magnetic Polarity. *mBio* **6**, e02286 (2015).
- 617 25. M. Toro-Nahuelpan, *et al.*, Segregation of prokaryotic magnetosomes organelles is driven by  
618 treadmilling of a dynamic actin-like MamK filament. *BMC Biol.* **14**, 88 (2016).
- 619 26. M. L. Ginger, N. Portman, P. G. McKean, Swimming with protists: perception, motility and  
620 flagellum assembly. *Nat. Rev. Microbiol.* **6**, 838–850 (2008).
- 621 27. D. Esquivel, H. Debarros, M. Farina, P. Aragao, J. Danon, Magnetotactic Microorganisms in the  
622 Rio-De-Janeiro Region. *Biol. Cell* **47**, 227–233 (1983).
- 623 28. M. Perantoni, *et al.*, Magnetic properties of the microorganism Candidatus Magnetoglobus  
624 multicellularis. *Naturwissenschaften* **96**, 685–690 (2009).
- 625 29. F. F. T. de Araujo, M. A. Pires, R. B. Frankel, C. E. M. Bicudo, Magnetite and Magnetotaxis in  
626 Algae. *Biophys. J.* **50**, 375–378 (1986).
- 627 30. P. Leão, *et al.*, Magnetosome magnetite biomineralization in a flagellated protist: evidence for an  
628 early evolutionary origin for magnetoreception in eukaryotes? *Environ. Microbiol.* **22**, 1495–1506  
629 (2019).
- 630 31. M. P. Pichel, T. A. G. Hageman, I. S. M. Khalil, A. Manz, L. Abelmann, Magnetic response of  
631 Magnetospirillum gryphiswaldense observed inside a microfluidic channel. *J. Magn. Magn. Mater.*  
632 **460**, 340–353 (2018).
- 633 32. C. Zahn, *et al.*, Measurement of the magnetic moment of single Magnetospirillum gryphiswaldense  
634 cells by magnetic tweezers. *Sci. Rep.* **7**, 1–14 (2017).
- 635 33. R. Nadkarni, S. Barkley, C. Fradin, A comparison of methods to measure the magnetic moment of  
636 magnetotactic bacteria through analysis of their trajectories in external magnetic fields. *PLoS ONE*  
637 **8**, e82064 (2013).
- 638 34. R. E. Dunin-Borkowski, *et al.*, Magnetic microstructure of magnetotactic bacteria by electron  
639 holography. *Science* **282**, 1868–1870 (1998).

- 640 35. F. Abreu, *et al.*, Cell adhesion, multicellular morphology, and magnetosome distribution in the  
641 multicellular magnetotactic prokaryote *Candidatus Magnetoglobus multicellularis*. *Microsc.*  
642 *Microanal. Off. J. Microsc. Soc. Am. Microbeam Anal. Soc. Microsc. Soc. Can.* **3**, 1–9 (2013).
- 643 36. P. Leão, *et al.*, Ultrastructure of ellipsoidal magnetotactic multicellular prokaryotes depicts their  
644 complex assemblage and cellular polarity in the context of magnetotaxis. *Environ. Microbiol.* **19**,  
645 2151–2163 (2017).
- 646 37. P. O. Conbhui, *et al.*, MERRILL: Micromagnetic Earth Related Robust Interpreted Language  
647 Laboratory. *Geochem. Geophys. Geosystems* **19**, 1080–1106 (2018).
- 648 38. L. Le Nagard, *et al.*, Magnetite magnetosome biomineralization in *Magnetospirillum magneticum*  
649 strain AMB-1: A time course study. *Chem. Geol.* **530**, 119348 (2019).
- 650 39. F. C. Meldrum, S. Mann, B. R. Heywood, R. B. Frankel, D. A. Bazylinski, Electron-microscopy  
651 study of magnetosomes in a cultured coccoid magnetotactic bacterium. *Proc. R. Soc. Lond. Ser. B-*  
652 *Biol. Sci.* **251**, 231–236 (1993).
- 653 40. F. C. Meldrum, S. Mann, B. R. Heywood, R. B. Frankel, D. A. Bazylinski, Electron-microscopy  
654 study of magnetosomes in 2 cultured vibrioid magnetotactic bacteria. *Proc. R. Soc. Lond. Ser. B-*  
655 *Biol. Sci.* **251**, 237–242 (1993).
- 656 41. M. Pósfai, C. T. Lefèvre, D. Trubitsyn, D. A. Bazylinski, R. B. Frankel, Phylogenetic significance  
657 of composition and crystal morphology of magnetosome minerals. *Front. Microbiol.* **4**, 344 (2013).
- 658 42. M. Winklhofer, L. G. Abraçado, A. F. Davila, C. N. Keim, H. G. P. Lins de Barros, Magnetic  
659 optimization in a multicellular magnetotactic organism. *Biophys. J.* **92**, 661–670 (2007).
- 660 43. C. T. Lefèvre, *et al.*, Monophyletic origin of magnetotaxis and the first magnetosomes. *Environ.*  
661 *Microbiol.* **15**, 2267–2274 (2013).
- 662 44. E. C. T. Descamps, J.-B. Abbé, D. Pignol, C. T. Lefèvre, “Controlled Biomineralization of  
663 Magnetite in Bacteria” in *Iron Oxides*, D. Faivre, Ed. (Wiley-VCH Verlag GmbH & Co. KGaA,  
664 2016), pp. 99–116.
- 665 45. R. B. Frankel, R. P. Blakemore, Navigational compass in magnetic bacteria. *J. Magn. Magn. Mater.*  
666 **15–8**, 1562–1564 (1980).
- 667 46. D. M. S. Esquivel, H. G. P. Lins De Barros, Motion of Magnetotactic Microorganisms. *J. Exp. Biol.*  
668 **121**, 153–163 (1986).
- 669 47. N. Petersen, D. G. Weiss, H. Vali, “Magnetic bacteria in lake sediments” in *Geomagnetism and*  
670 *Palaeomagnetism*, NATO ASI Series., F. J. Lowes, *et al.*, Eds. (Springer Netherlands, 1989), pp.  
671 231–241.
- 672 48. Y. Pan, *et al.*, Reduced efficiency of magnetotaxis in magnetotactic coccoid bacteria in higher than  
673 geomagnetic fields. *Biophys. J.* **97**, 986–991 (2009).
- 674 49. E. Wajnberg, L. Desouza, H. Debarros, D. Esquivel, A Study of Magnetic-Properties of  
675 Magnetotactic Bacteria. *Biophys. J.* **50**, 451–455 (1986).

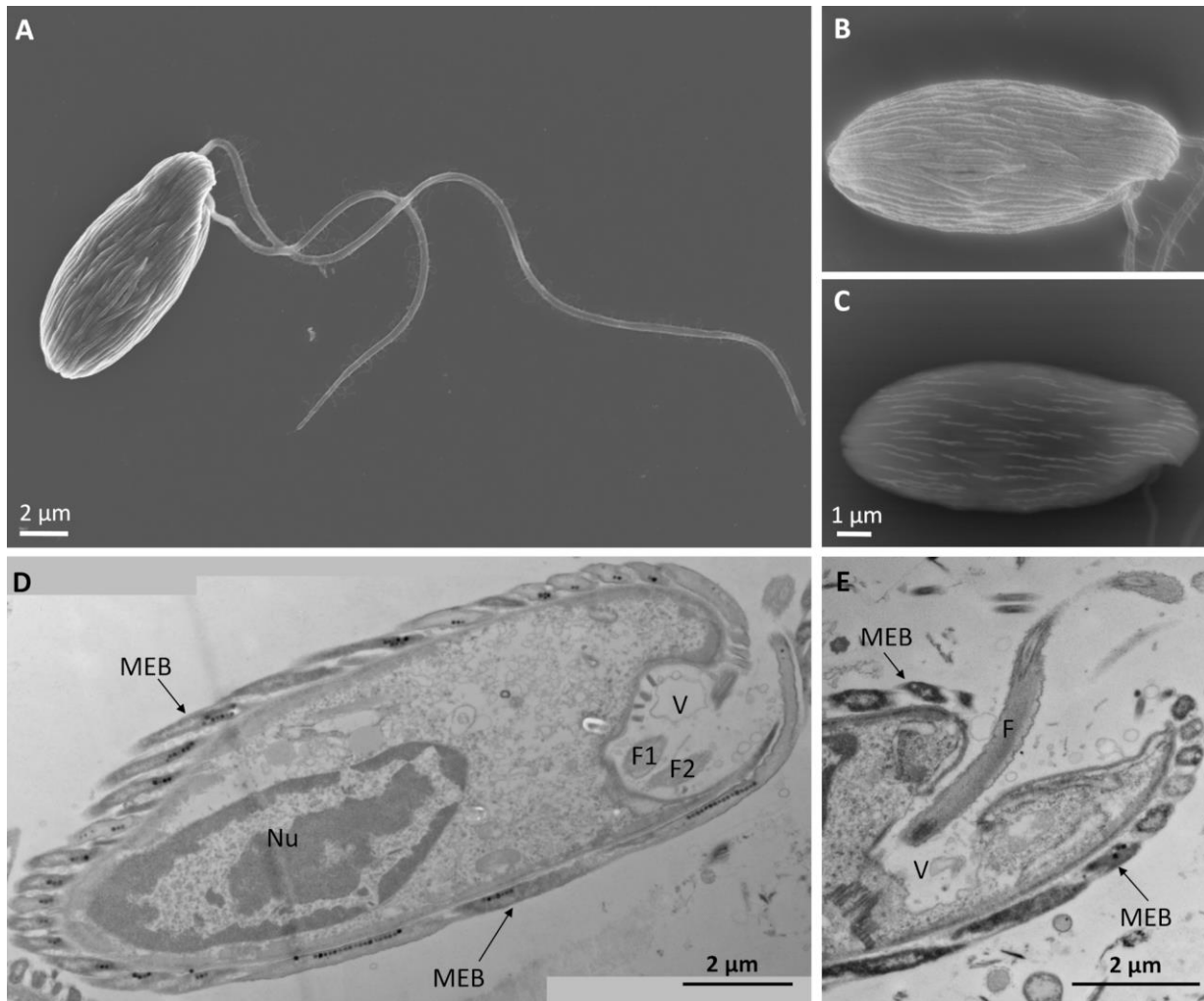
- 676 50. S. S. Kalirai, D. A. Bazylinski, A. P. Hitchcock, Anomalous magnetic orientations of magnetosome  
677 chains in a magnetotactic bacterium: *Magnetovibrio blakemorei* strain MV-1. *PLoS One* **8**, e53368  
678 (2013).
- 679 51. E. F. DeLong, R. B. Frankel, D. A. Bazylinski, Multiple evolutionary origins of magnetotaxis in  
680 bacteria. *Science* **259**, 803–806 (1993).
- 681 52. W. Lin, *et al.*, Origin of microbial biomineralization and magnetotaxis during the Archean. *Proc.*  
682 *Natl. Acad. Sci. U. S. A.* **114**, 2171–2176 (2017).
- 683 53. J. M. Byrne, *et al.*, Redox cycling of Fe(II) and Fe(III) in magnetite by Fe-metabolizing bacteria.  
684 *Science* **347**, 1473–1476 (2015).
- 685 54. V. P. Edgcomb, *et al.*, Identity of epibiotic bacteria on symbiontid euglenozoans in O<sub>2</sub>-depleted  
686 marine sediments: evidence for symbiont and host co-evolution. *ISME J.* **5**, 231–243 (2011).
- 687 55. F. F. Guo, *et al.*, Magnetosomes eliminate intracellular reactive oxygen species in *Magnetospirillum*  
688 *gryphiswaldense* MSR-1. *Environ. Microbiol.* **14**, 1722–1729 (2012).
- 689 56. K. Li, *et al.*, Magnetosomes extracted from *Magnetospirillum magneticum* strain AMB-1 showed  
690 enhanced peroxidase-like activity under visible-light irradiation. *Enzyme Microb. Technol.* **72**, 72–  
691 78 (2015).
- 692 57. T. Fenchel, B. Finlay, Oxygen and the spatial structure of microbial communities. *Biol. Rev. Camb.*  
693 *Philos. Soc.* **83**, 553–569 (2008).
- 694 58. D. Schüler, E. Baeuerlein, Dynamics of iron uptake and Fe<sub>3</sub>O<sub>4</sub> biomineralization during aerobic  
695 and microaerobic growth of *Magnetospirillum gryphiswaldense*. *J. Bacteriol.* **180**, 159–162 (1998).
- 696 59. R. B. Frankel, D. A. Bazylinski, M. S. Johnson, B. L. Taylor, Magneto-aerotaxis in marine coccoid  
697 bacteria. *Biophys. J.* **73**, 994–1000 (1997).
- 698 60. N. Philippe, L.-F. Wu, An MCP-like protein interacts with the MamK cytoskeleton and is involved  
699 in magnetotaxis in *Magnetospirillum magneticum* AMB-1. *J. Mol. Biol.* **400**, 309–322 (2010).
- 700 61. D. Schüler, The biomineralization of magnetosomes in *Magnetospirillum gryphiswaldense*. *Int.*  
701 *Microbiol. Off. J. Span. Soc. Microbiol.* **5**, 209–214 (2002).
- 702 62. M. Bennet, *et al.*, Influence of Magnetic Fields on Magneto-Aerotaxis. *PLoS ONE* **9**, e101150  
703 (2014).
- 704 63. A. Sorrentino, *et al.*, MISTRAL: a transmission soft X-ray microscopy beamline for cryo nano-  
705 tomography of biological samples and magnetic domains imaging. *J. Synchrotron Radiat.* **22**, 1112–  
706 1117 (2015).
- 707 64. J. Otón, *et al.*, Characterization of transfer function, resolution and depth of field of a soft X-ray  
708 microscope applied to tomography enhancement by Wiener deconvolution. *Biomed. Opt. Express* **7**,  
709 5092–5103 (2016).

- 710 65. I. Belevich, M. Joensuu, D. Kumar, H. Vihinen, E. Jokitalo, Microscopy Image Browser: A  
711 Platform for Segmentation and Analysis of Multidimensional Datasets. *PLOS Biol.* **14**, e1002340  
712 (2016).
- 713 66. D. Stalling, M. Westerhoff, H.-C. Hege, “38 - amira: A Highly Interactive System for Visual Data  
714 Analysis” in *Visualization Handbook*, C. D. Hansen, C. R. Johnson, Eds. (Butterworth-Heinemann,  
715 2005), pp. 749–767.
- 716 67. R. Belkhou, *et al.*, HERMES: a soft X-ray beamline dedicated to X-ray microscopy. *J. Synchrotron*  
717 *Radiat.* **22**, 968–979 (2015).
- 718 68. S. Swaraj, *et al.*, Performance of the HERMES beamline at the carbon K-edge. *J. Phys. Conf. Ser.*  
719 **849**, 012046 (2017).

720

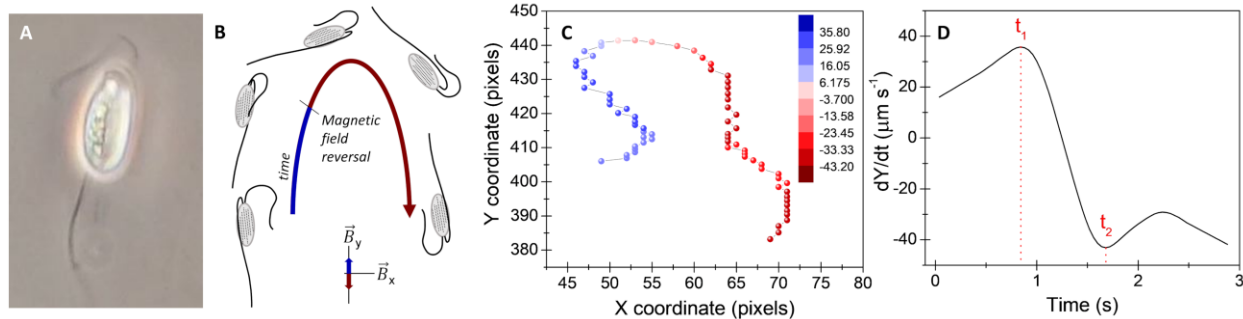
721

722 **Figures legend**



723  
724 **Fig. 1. Observation of the motility apparatus of MHBs isolated from Carry-le-Rouet, France.** (A-C)  
725 SEM images of cells prepared using a critical-point drying approach showing (A) a whole MHB, (B) a  
726 higher magnification of the same holobiont observed at 2 kV showing the surface of the holobiont, and (C)  
727 the same as in (B) but observed at 10 kV using the backscattered mode showing the magnetosome chains  
728 inside the ectosymbiotic bacteria. (D) Stitched TEM images of longitudinal ultrathin sections of a MHB  
729 showing the vestibulum on the front of the protistan cells and the two flagella and (E) TEM image showing  
730 one flagellum emerging from this cavity. Nu: nucleus; MEB: magnetic ectosymbiotic bacteria; F: flagella;  
731 V: vestibulum.

732



733

734 **Fig. 2. Observation of the magnetic response of MHBs isolated from Carry-le-Rouet, France.** (A)

735 Optical microscopy image of a swimming MHB showing the position of the flagella. (B) Schematic of U-

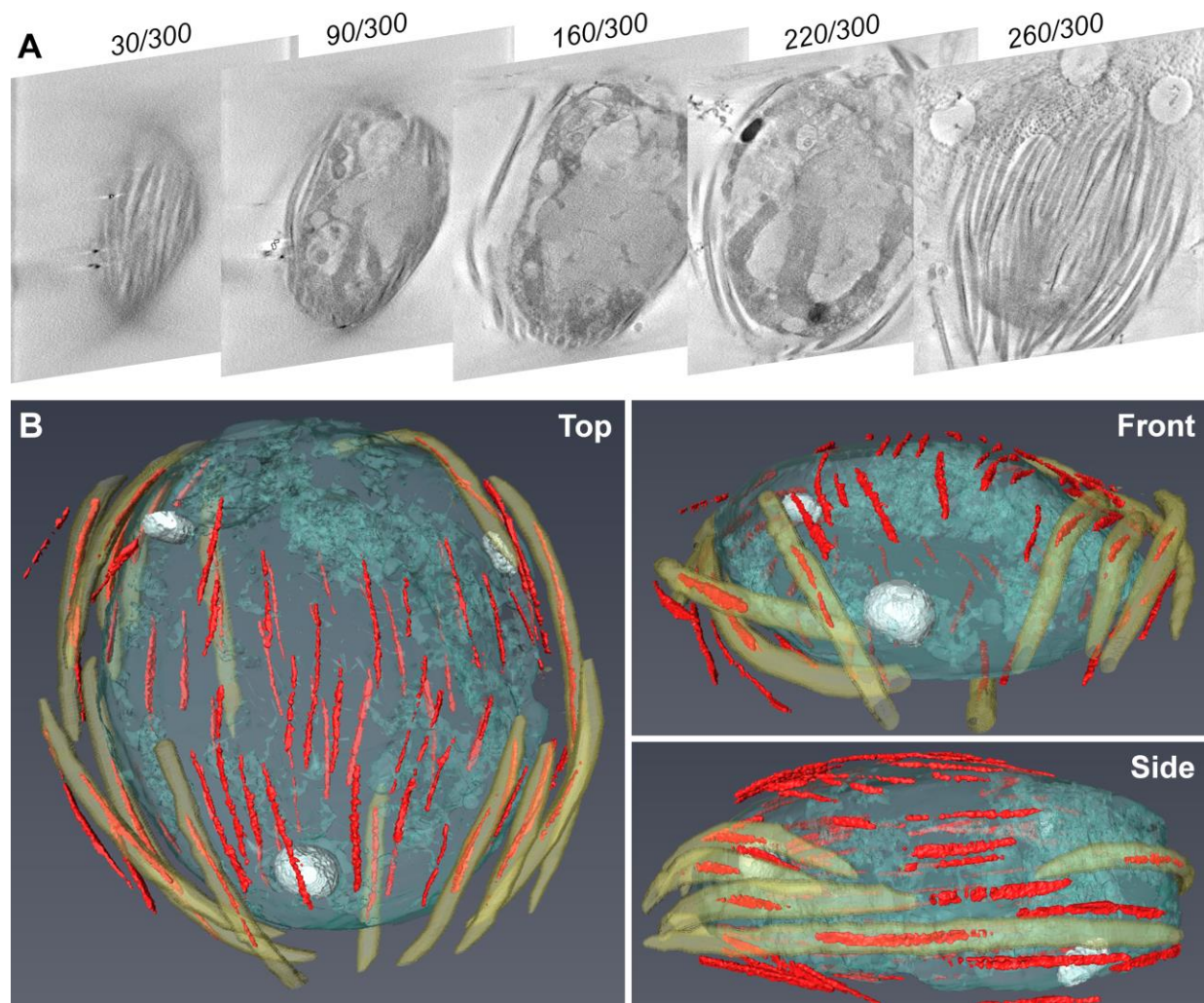
736 turn trajectory measurements during magnetic field reversal. (C) The trajectory plot of a U-turn at 3.5 mT

737 magnetic field switching. The instantaneous velocity ( $\mu\text{m}\cdot\text{s}^{-1}$ ) is represented in color indicating the MHB

738 motility direction where the blue color indicates upwards motion and red color the downward displacement.

739 (D) Time difference subtracted from first derivate peaks ( $t_1$  and  $t_2$ ) of the Y trajectory to yield  $\tau_{\text{Uturn}}$ .

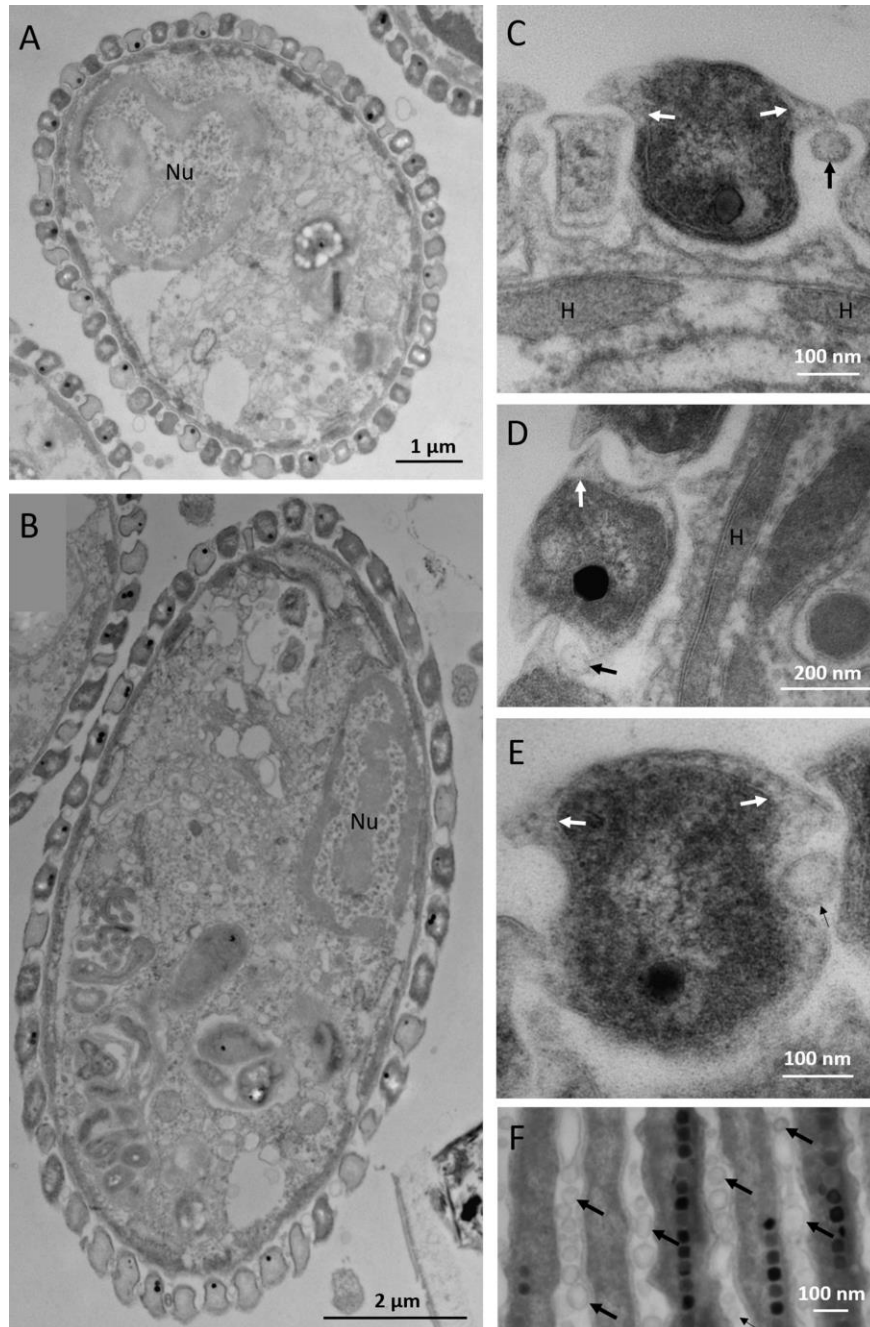
740



741

742 **Fig. 3. 3-D reconstruction of vitrified MHB using cryo soft X-ray tomography (cryo-SXT).** (A) Virtual  
 743 slices of X-ray tomography reconstruction through the Z-direction from top to bottom of MHB (see Movie  
 744 S2). (B) Volume reconstruction of magnetosome chains (red), ectosymbiotic bacteria membrane (yellow),  
 745 the protistan host (cyan) and dense intracellular granules (white) from different viewpoints.

746



747

748 **Fig. 4. Organization and attachment of ectosymbiotic bacteria at the surface of their host.**

749 Transmission electron microscope images in bright field mode of ultrathin sections of MHB showing (A,B)

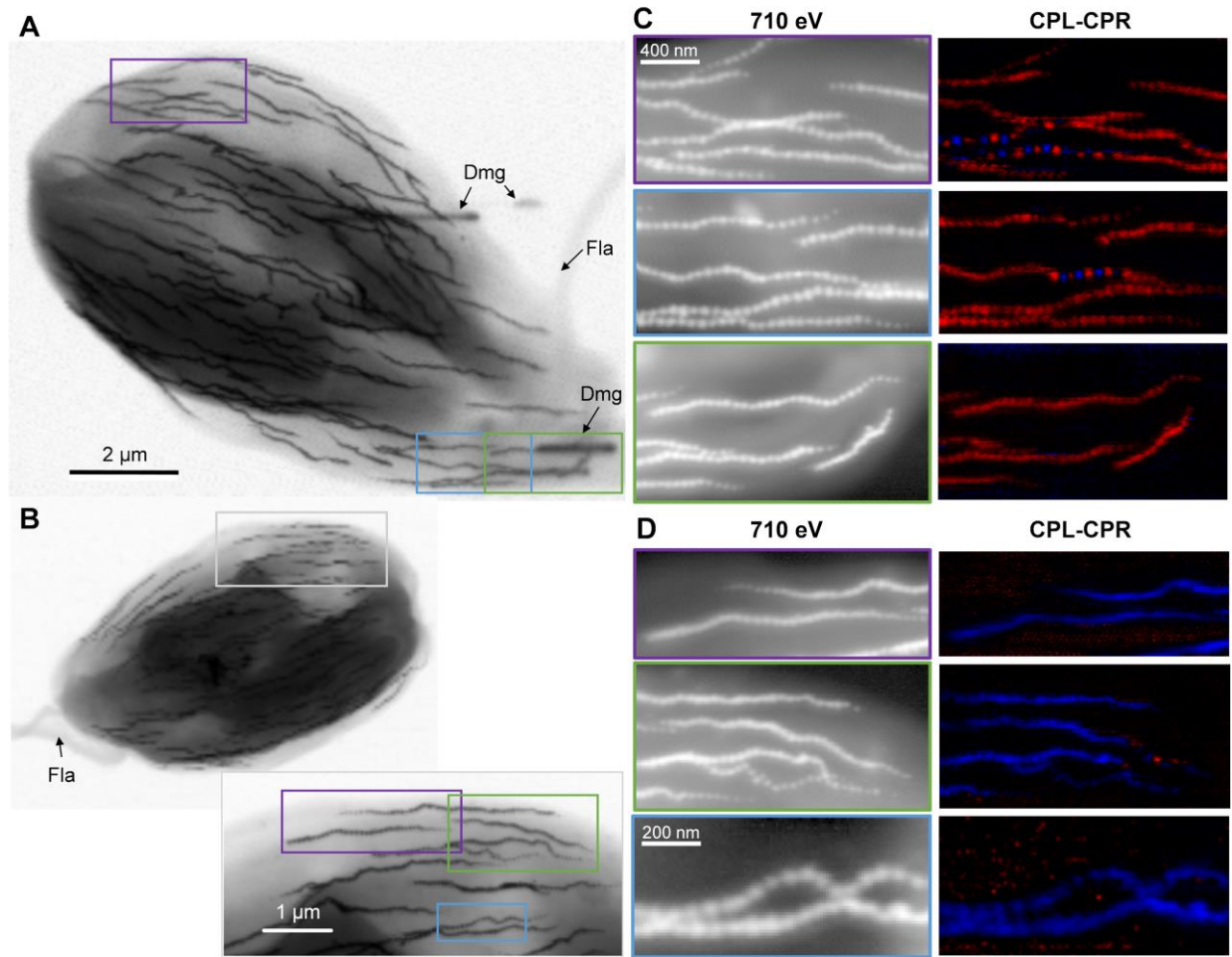
750 the presence of only one layer of bacteria at the surface of their host, (C) the presence of bacteria in channels

751 formed at the surface of their host, (C,D) the proximity of ectosymbionts with hydrogenosomes, (C-E, white

752 arrows) the wing-like structures that are outgrowths of bacterial external membrane, and (C-F, black

753 arrows) the presence of vesicles between the bacteria. Nu: nucleus; H: hydrogenosomes. All are transverse

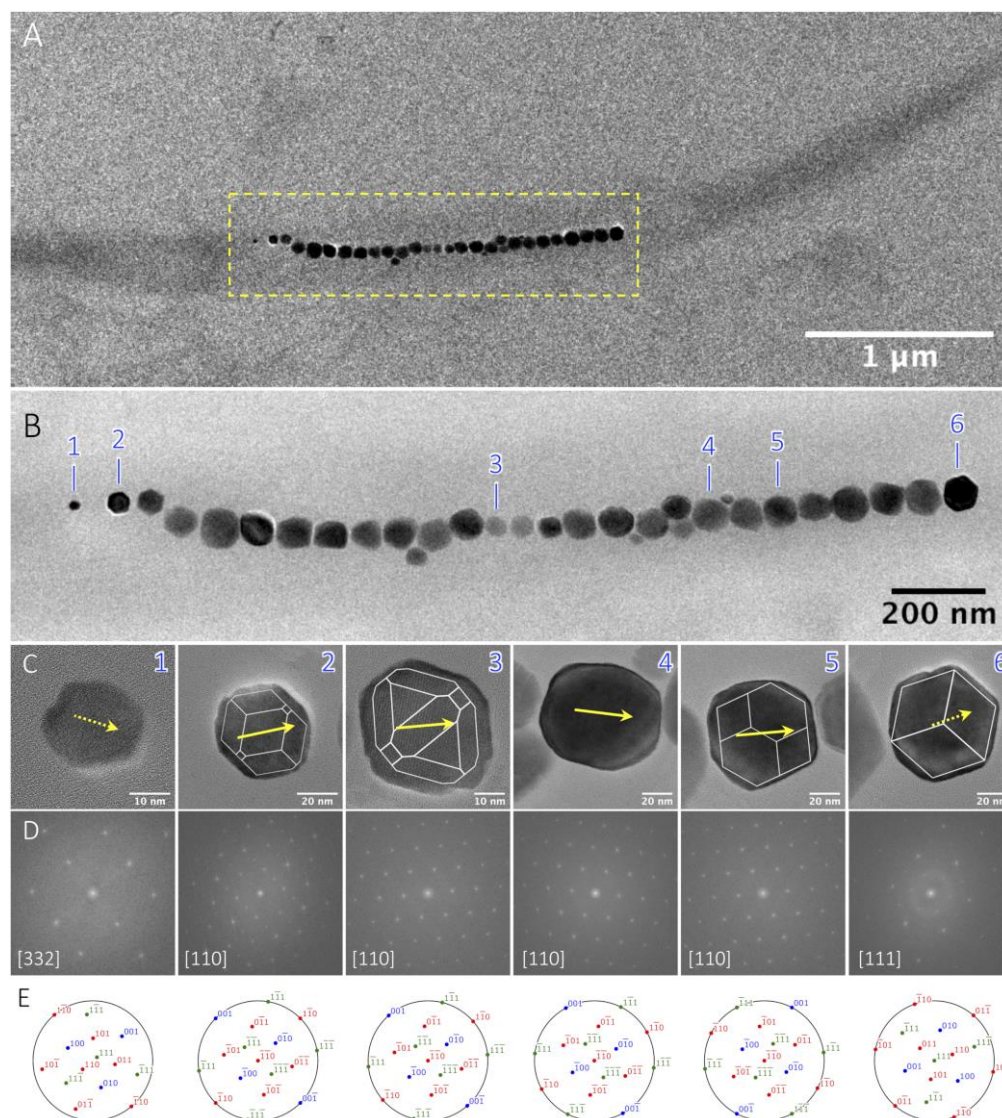
754 sections except for F, which is longitudinal.



755

756 **Fig. 5. Magnetic moment orientation of magnetosomes relative to the protistan flagella using soft X-**  
 757 **ray scanning transmission X-ray microscopy (STXM) at the Fe L-edge and X-ray magnetic circular**  
 758 **dichroism (XMCD) without applied magnetic fields. (A,B) STXM images at 710 eV of MHB deposited**  
 759 **in opposite directions. Fla: flagella; Dmg: X-ray beam damage from previous scans. Colored frames**  
 760 **indicate the regions further analyzed. (C,D) Optical density maps (left-side panels) and difference maps of**  
 761 **circular polarization left (CPL) and circular polarization right (CPR) at 708.8 eV (where maximum XMCD**  
 762 **signal was found) (right-side panels).**

763



764

765 **Fig. 6. Crystallography of the cuboctahedral/prismatic magnetite particles produced by a magnetic**

766 **ectosymbiotic bacteria.** (A) Transmission electron microscope bright-field (TEM-BF) image of a magnetic

767 ectosymbiotic bacterium detached from its host and its single magnetosome chain (B).

768 (C) High-resolution transmission electron microscopy (HR-TEM) images of the crystals annotated 1-6 in (B). Prismatic models

769 drawn in white were superimposed on the image of these crystals with an acceptable match. Yellow arrows

770 indicate the  $\langle 111 \rangle$  direction: plain arrows correspond to in plane direction and dashed arrows are related

771 to out-of-plane direction (for the latter, smaller arrow length corresponds to a higher out-of-plane angle).

772 (D) FFT pattern of these HR-TEM indexed with the magnetite structure (spacegroup  $Fm\bar{3}m$ ,  $a = 8.04 \text{ \AA}$ ).

773 (E) Stereographic projection oriented with respect to the orientation inferred from (D) using SingleCrystal

774 software. The orientations of the models and the  $\langle 111 \rangle$  directions were deduced from the stereographic

775 projections.

776 **Supporting Information for**

777

778 **Collective magnetotaxis of microbial holobionts is optimized by the three-**  
779 **dimensional organization and magnetic properties of ectosymbionts**

780 Daniel M. Chevrier<sup>1\*</sup>, Amélie Juhin<sup>2</sup>, Nicolas Menguy<sup>2</sup>, Romain Bolzoni<sup>1</sup>, Paul E. D. Soto-Rodriguez<sup>1</sup>,  
781 Mila Kojadinovic-Sirinelli<sup>1</sup>, Greig A. Paterson<sup>3</sup>, Rachid Belkhou<sup>4</sup>, Wyn Williams<sup>5</sup>, Fériel Skouri-Panet<sup>2</sup>,  
782 Artemis Kosta<sup>6</sup>, Hugo Le Guenno<sup>6</sup>, Eva Pereiro<sup>7</sup>, Damien Faivre<sup>1</sup>, Karim Benzerara<sup>2</sup>, Caroline L. Monteil<sup>1</sup>,  
783 Christopher T. Lefevre<sup>1\*</sup>

784

785 \*Corresponding author: Drs. Daniel Chevrier and Christopher T. Lefevre

786 Emails: daniel.chevrier@cea.fr and christopher.lefevre@cea.fr This PDF file includes:

787

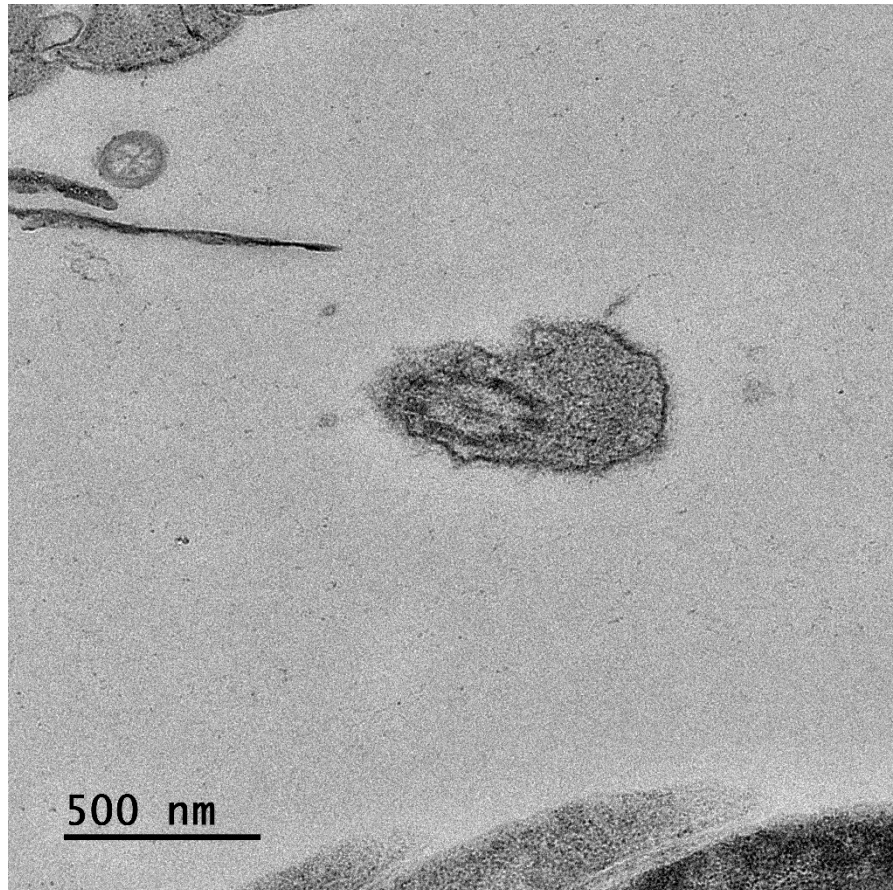
788 Figs. S1 to S15

789 Movie S1. Light microscope movie of south-seeking magnetotactic holobionts sampled from Carry-le-  
790 Rouet, Mediterranean Sea, showing the motility of the consortium and the presence of two flagella  
791 emerging from the front of the protistan host.

792 Movie S2. Reconstructed tomogram of MHB from cryo-transmission X-ray microscopy (cTXM) imaging.  
793 Video depicts the volume contents by traversing the Z-direction.

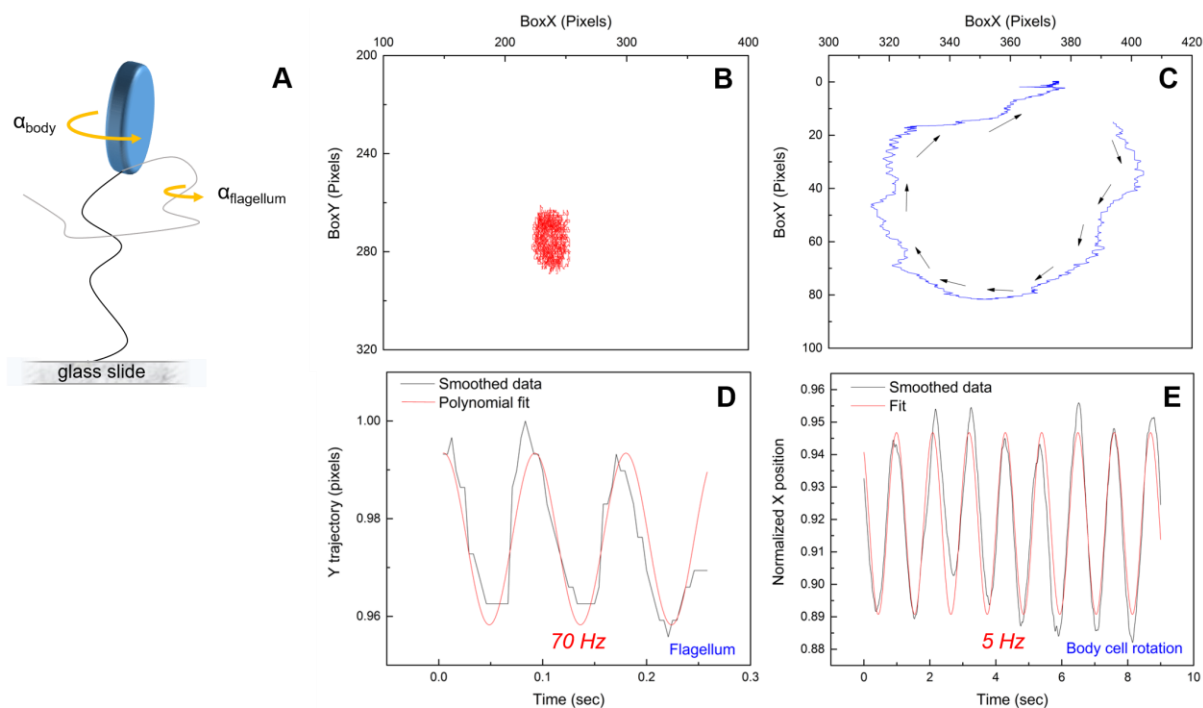
794

795  
796  
797  
798  
799



800  
801  
802  
803  
804

**Fig. S1.** Transmission electron microscope image of the transversal section of a flagellum of a protist carrying magnetic ectosymbiotic bacteria showing a canonical '9+2' microtubule axoneme structure.



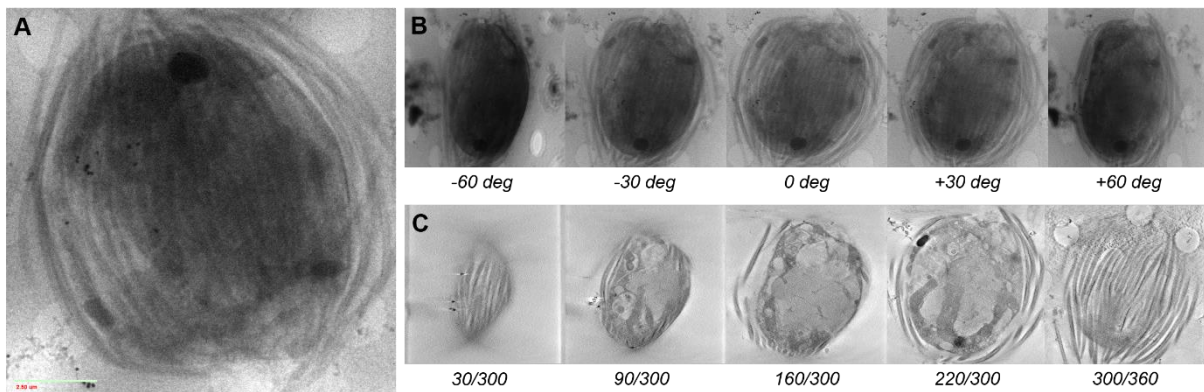
806

807 **Fig. S2. Motility and magnetotactic behavior of MHBs.** The swimming behavior of MHBs was  
 808 investigated with live microscopy imaging within a framework of Helmholtz coils to control the local  
 809 magnetic field strength around the specimen (Materials and Methods). (A) Model depiction of MHBs  
 810 attached to the glass slide with one of their two flagella. A few instances of this provided an opportunity to  
 811 estimate the rotational speed of the cell body ( $\alpha_{\text{body}}$ ) and flagellum ( $\alpha_{\text{flagellum}}$ ). (B) An example of the tracked  
 812 rotation of the cell body of attached MHB which allowed tracking of flagella rotation. (C) Example of 2D  
 813 MHB trajectory when unbound and swimming close to glass slide surface, showing a circular motion with  
 814 helicoidal motility where the cell body is rotating around its longitudinal axis. The mean cell velocity of  
 815 freely-swimming MHBs in the bulk liquid (away from glass slide surface) was determined to be  $107 \mu\text{m}\cdot\text{s}^{-1}$ ,  
 816 with a maximum of  $155 \mu\text{m}\cdot\text{s}^{-1}$  ( $n = 16$ ). The rotational axis is parallel to the swimming trajectory during  
 817 the entire swimming motion (see Movie S1). It was observed that a single in-plane rotation corresponds to  
 818 one single body cell rotation, thus by tracking the in-plane circular motion the body rotation frequency can  
 819 be extracted. By fitting extracted coordinate positions versus time Fig. 2B and 2C with  $X=X_0+A\cos(\omega t)$ ,  
 820 frequencies ( $f=\omega/2\pi$ ) of (D) *ca.* 70 Hz for the flagellum and (E) *ca.* 5 Hz for the body cell are obtained for  
 821 example.

822

823

824



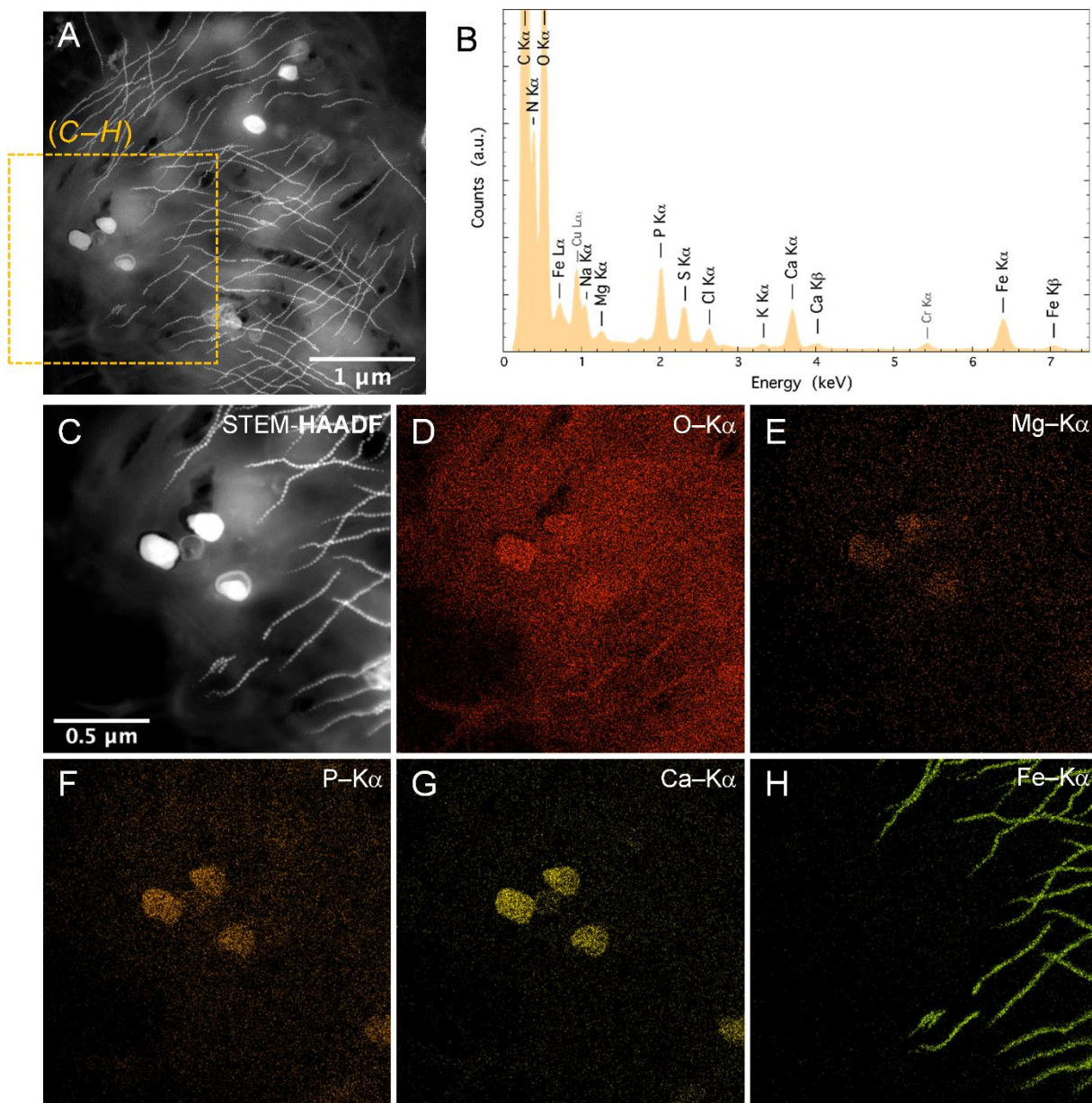
825

826 **Fig. S3. Cryo soft X-ray tomography (cryo-SXT) of a MHB.** (A) Raw X-ray image of MHB at 520 eV.

827 (B) Tilt-series images and (C) reconstructed virtual slices (in Z-direction) of X-ray tomography data.

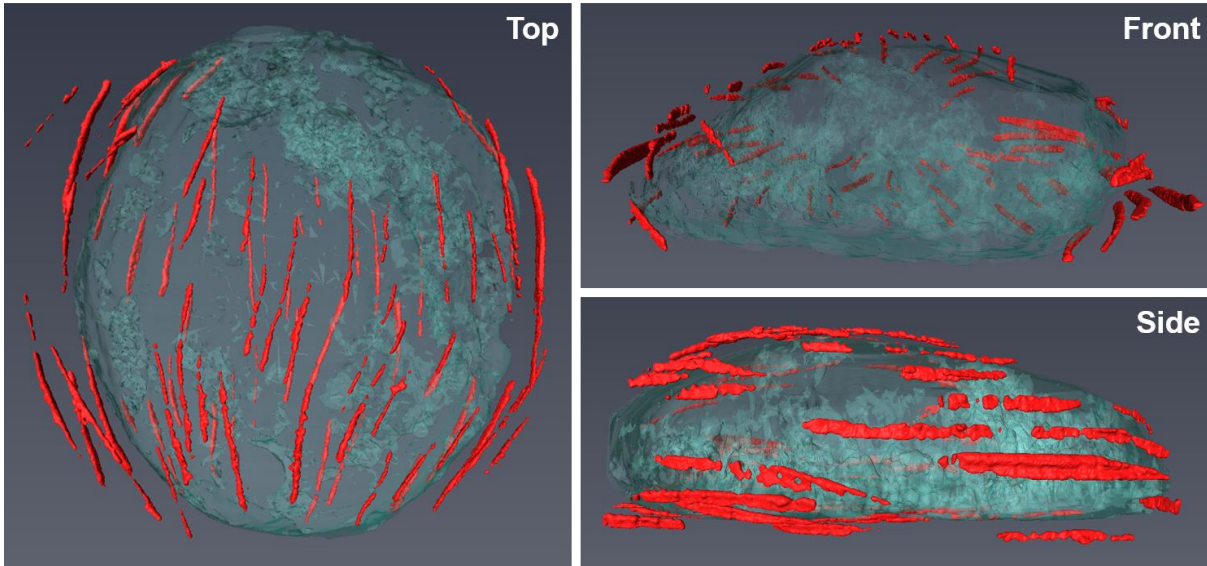
828

829



830

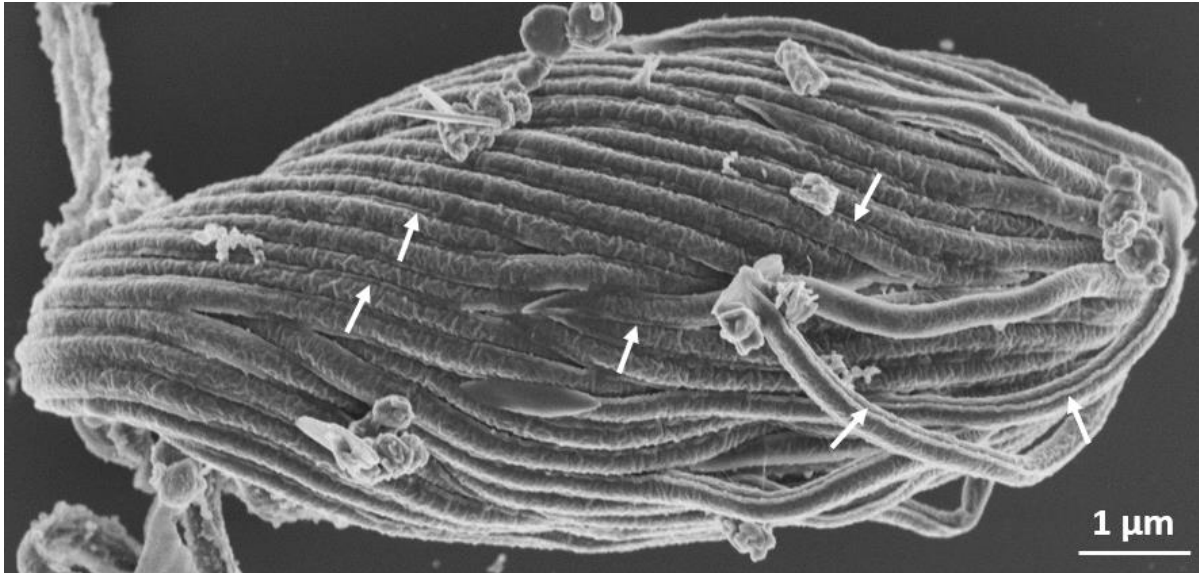
831 **Fig. S4. Chemical identification of the inclusions found in MHBs.** (A) STEM-HAADF image of an  
 832 unfixed MHB. The dashed square corresponds to the region further analyzed. (B) XEDS elemental spectrum  
 833 of an inclusion. (C) STEM-HAADF image of the region shown in (A) by a dashed square. XEDS elemental  
 834 mapping of oxygen (D), magnesium (E), phosphorus (F), calcium (G) and iron (H).



835

836 **Fig. S5.** 3-D volume reconstruction of magnetosome chains (red) and protistan host (cyan) from X-ray  
837 tomography (cryo-SXT) data.

838

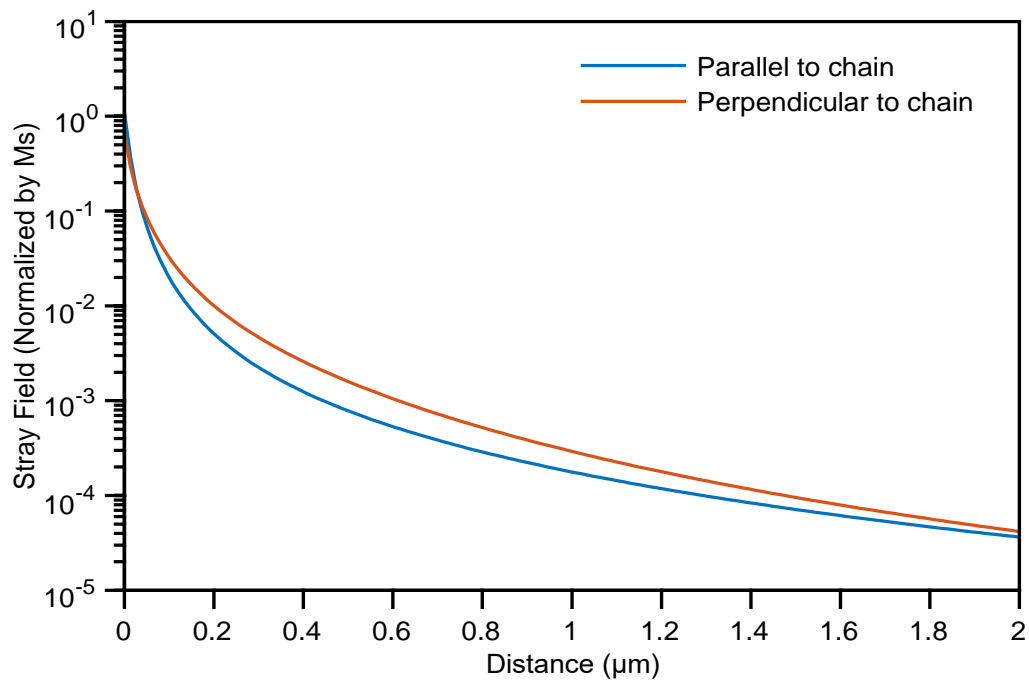


839

840 **Fig. S6.** SEM image of a MHB prepared using a critical-point drying approach showing the presence of  
841 lines between each neighbor magnetic ectosymbiotic bacteria or two lines on the side of each bacteria  
842 detached from the host (i.e. white arrows). These lines correspond to the wing-like structures observed on  
843 transversal thin-sectioned bacteria observed on TEM (Fig. 4C-E). Note that although it was fixed, this  
844 holobiont suffers from the preparation explaining the partial detachment and misalignment of some  
845 ectosymbiotic bacteria from their host.

846

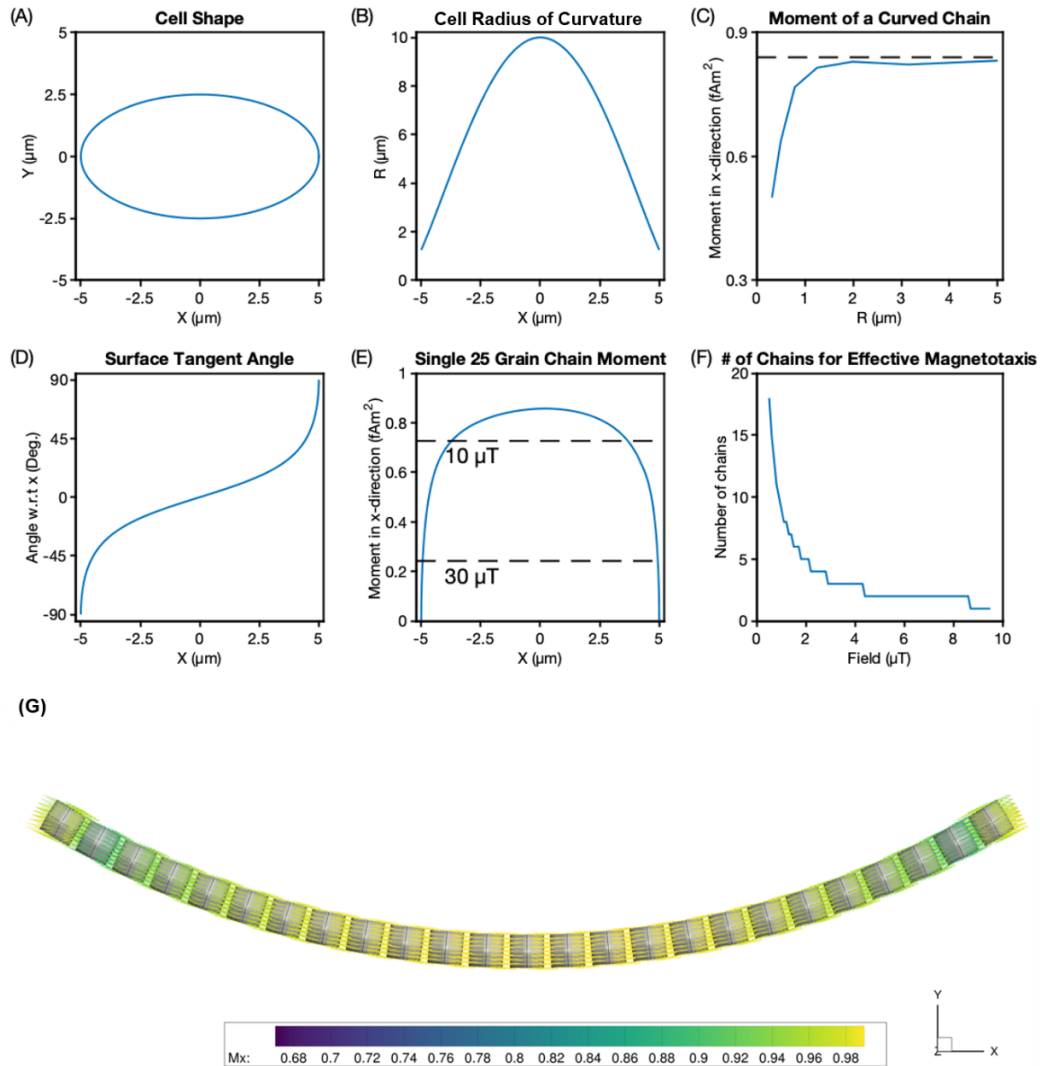
847



848

849 **Fig. S7.** Micromagnetic simulations of a modelled magnetosome chain from MHB (25 rhomboidal  
850 dodecahedral particles with a mid-sphere diameter of 60 nm and 10 nm spacing between particles) showing  
851 the stray fields adjacent to the chain.

852



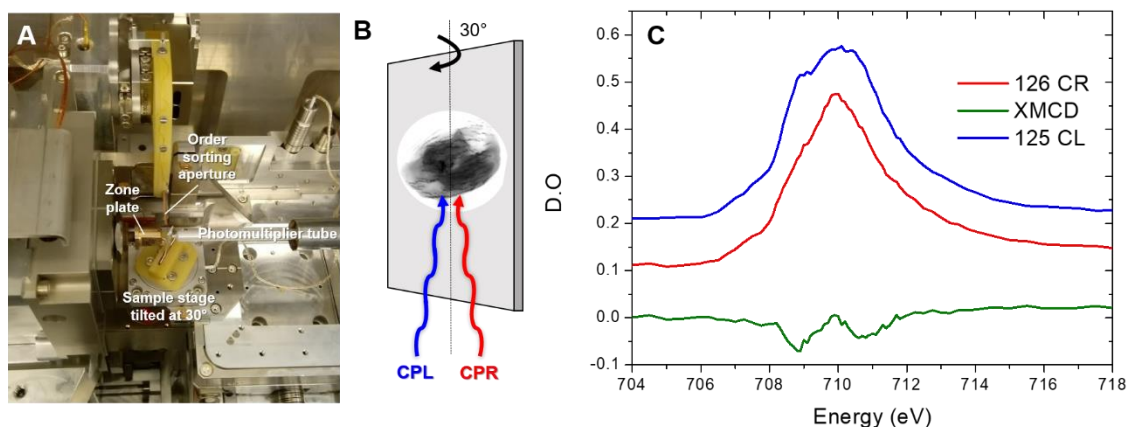
853

854 **Fig. S8.** Calculations to determine the net moment of a protist cell with chains of 25 rhomboidal  
 855 dodecahedral magnetosomes (with a mid-sphere diameter of 60 nm and spacing of 10 nm) at various  
 856 degrees of chain curvature. (A) The dimensions of a prolate cross-section of a protist cell. (B) The radius of  
 857 curvature of the cell as a function of long axis position. (C) The net x-direction magnetic moment of the  
 858 magnetosome chain with increasing radius of curvature (Note: as the radius increases the degree of chain  
 859 bending decreases). (D) The angle of the surface tangent with respect to the x-direction. (E) The net x-  
 860 direction moment of a single magnetosome chain as a function of long axis position accounting for the cell  
 861 curvature and tangential angle with respect to the x-direction. The horizontal dashed lines indicate the  
 862 magnetic moments at which the characteristic timescales of magnetic torque rotation and Brownian motion  
 863 (at 20 °C) are equal in fields of 10 or 30  $\mu\text{T}$ . (F) The minimum number of chains for effective magnetotaxis  
 864 as a function of field. One chain near the middle of the cell is sufficient to overcome Brownian motion in  
 865  $\sim 10 \mu\text{T}$  and 2-3 chains would be sufficient to impart a significant magnetotactic advantage over other  
 866 similarly sized organisms. In extremely weak fields ( $\sim 1 \mu\text{T}$ ) about nine chains are required to overcome  
 867 Brownian effects. (G) An example micromagnetic calculation for the chain of 25 magnetosomes. The chain  
 868 is curved around a circle of radius  $1.25 \mu\text{m}$ . Magnetic moment vectors are colored according to percentage  
 869 of maximum alignment (0.00 to 1.00) with the x-direction ( $M_x$ ).

870

871

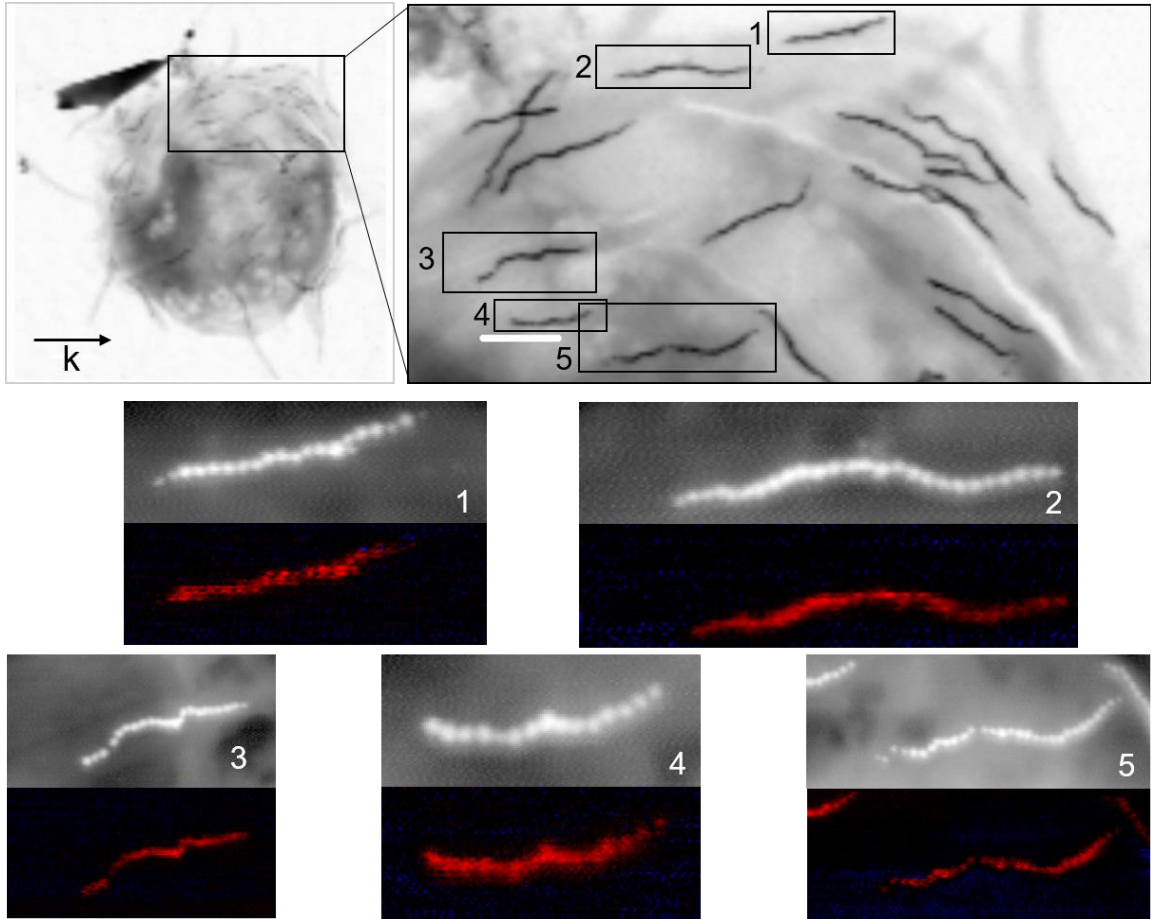
872



873

874 **Fig. S9.** (A) Scanning transmission X-ray microscopy (STXM) experimental sample environment for X-  
875 ray magnetic circular dichroism (XMCD) measurement. (B) Depiction of 30 deg tilt to measure the intrinsic  
876 XMCD signal of the MHB sample, where the magnetosome chains are perpendicular to the axis of rotation.  
877 (C) Example of Fe L<sub>3</sub>-edge XAS spectra recorded with right (CPR)- and left (CPL)-circularly polarized X-  
878 rays with the difference spectra or XMCD signal. XAS spectra highly resemble magnetite and  
879 magnetosomes materials as found in other STXM-XMCD studies (1, 2).

880

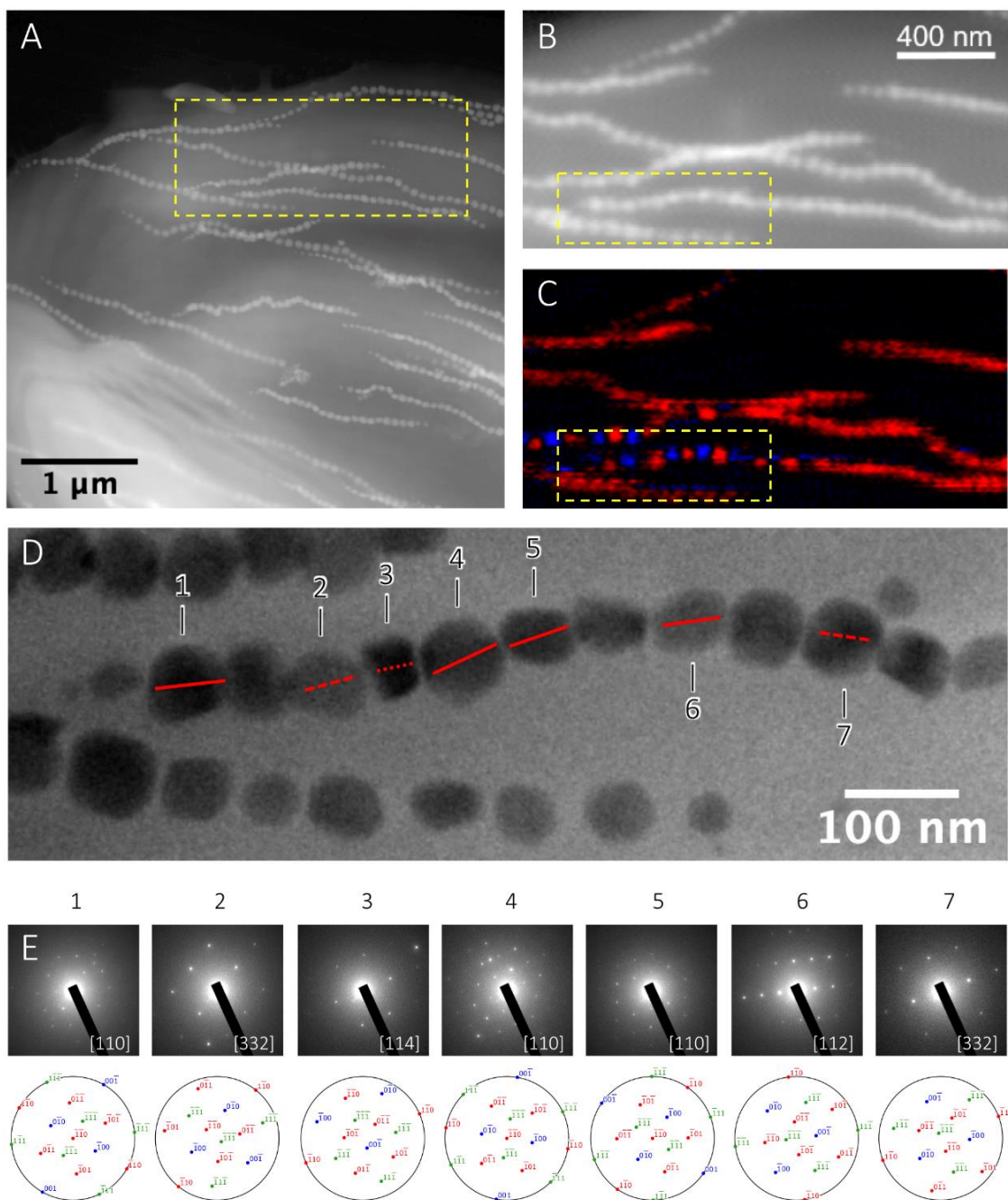


881

882 **Fig. S10.** Scanning transmission X-ray microscopy (STXM) images of unfixed MHB at 710 eV (above)  
 883 with X-ray magnetic circular dichroism (XMCD) maps (OD-corrected and CPL-CPR images at 708.8 eV)  
 884 of individual magnetosome chains (below).

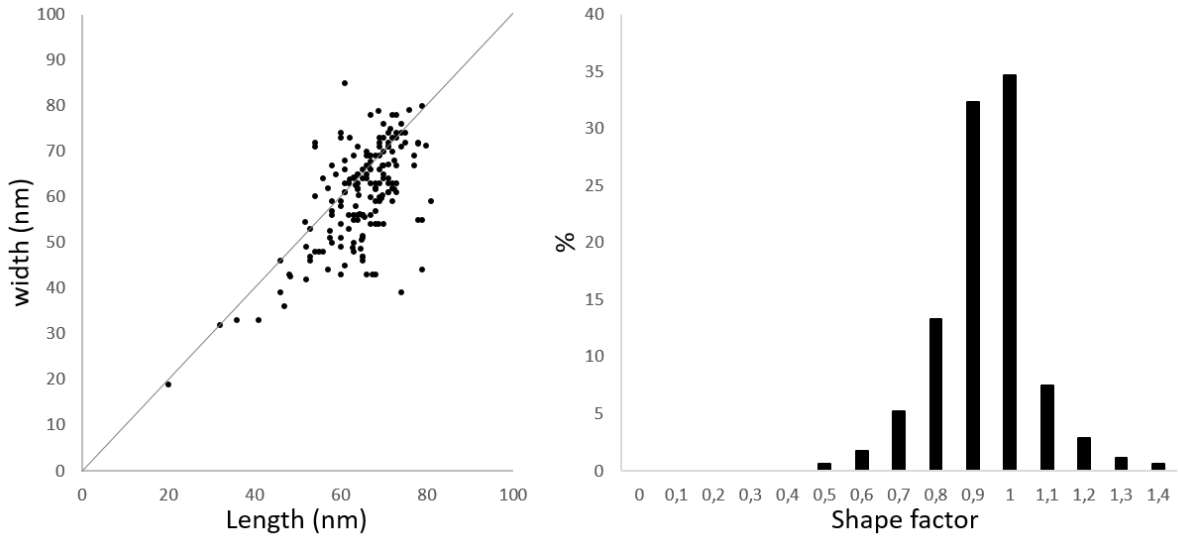
885

886



887

888 **Fig. S11.** (A-B) Scanning transmission electron microscopy high-angle annular dark field (STEM-HAADF)  
 889 images of the region where individual magnetite nanocrystal magnetic dipoles invert (Fig. 5A (top left) and  
 890 C (top right)) showing the morphology and organization of magnetosomes. Dashed frames indicate the  
 891 regions further analyzed. (C) Difference maps of circular polarization left (CPL) at 708.8 eV showing two  
 892 magnetosome chains extremity with inversion of individual magnetic dipole direction.. (D) Transmission  
 893 electron microscope bright-field (TEM-BF) image of the dashed region in (C) containing magnetosomes  
 894 with inversion of individual magnetic dipole direction. Red lines across selected magnetosome particles  
 895 indicate the  $\langle 111 \rangle$  direction as determined in (E) from single particle diffraction, with fast Fourier  
 896 transform (FFT) and stereographic projections shown below for each particle.



897

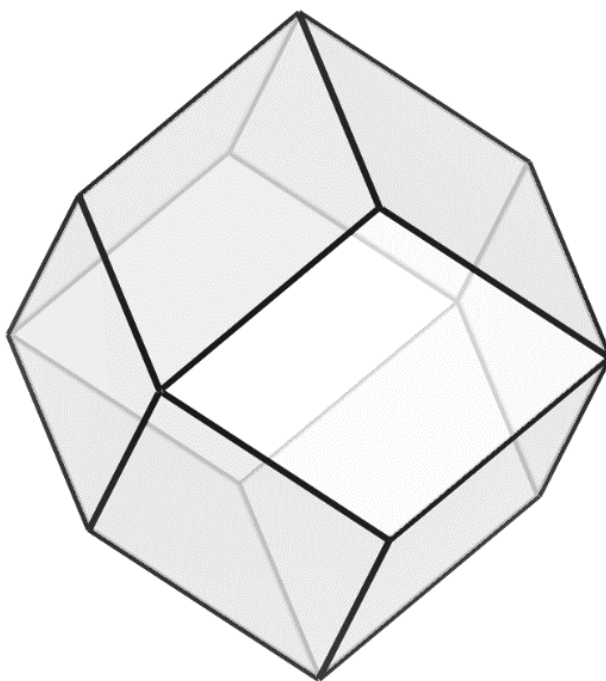
898 **Fig. S12.** Width versus length and crystal shape factor distribution of magnetic ectosymbiotic bacteria  
 899 showing a general trend of cuboctahedral particles. 173 magnetosomes from several ectosymbionts and  
 900 three different MHB were measured, considering the size of the particle parallel to the chain, the length and  
 901 the size of the particle perpendicular to the chain, the width. An average length and width of  $65 \pm 9$  nm and  
 902  $60 \pm 11$  nm, respectively, was found. The shape factor (width/length) was  $0.93 \pm 0.13$ . These results are  
 903 consistent with analyses of cuboctahedral/prismatic particles from environmental or cultivated MTB (3–6).

904

905

906

907

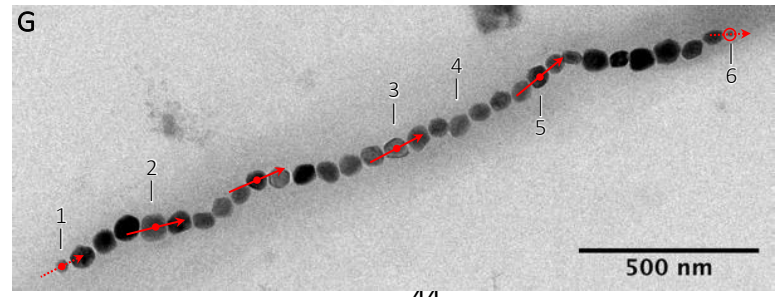
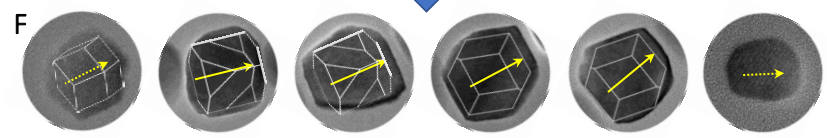
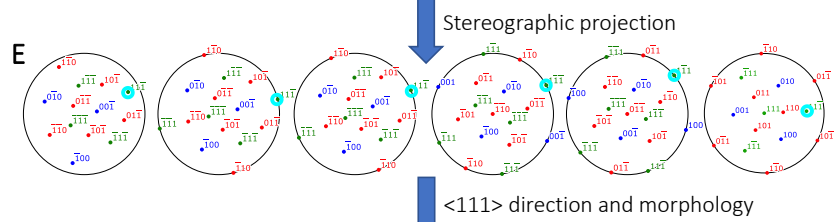
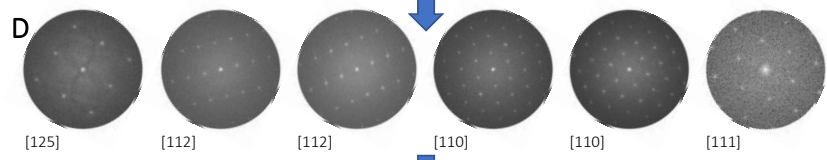
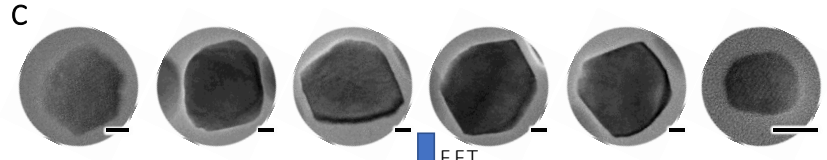
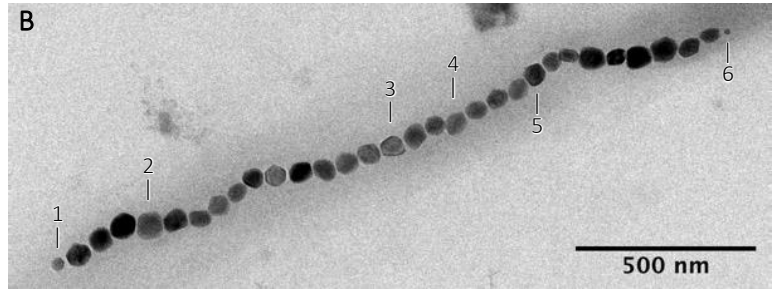
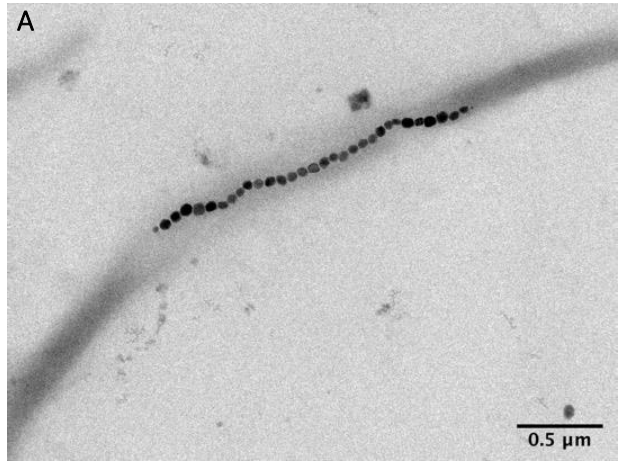


908

909 **Fig. S13.** Proposed crystallographic shape of magnetite nanocrystals as measured by high-resolution  
910 transmission electron microscopy (Fig. 6, Fig. S14 and S15).

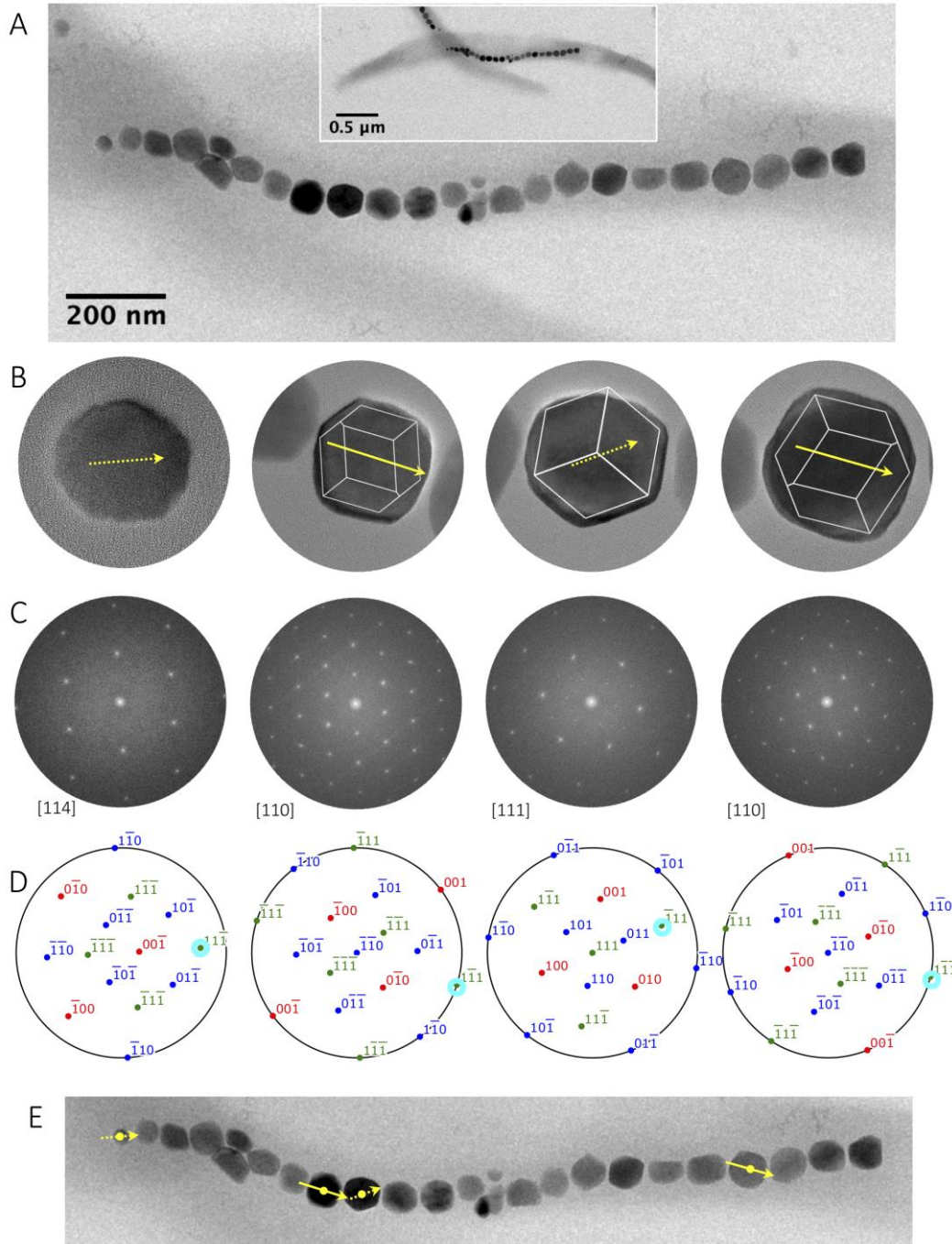
911

912



914 **Fig. S14. Crystallography of the prismatic/cuboctahedral magnetite particles produced by magnetic**  
915 **ectosymbiotic bacteria.** (A) Transmission electron microscope bright-field (TEM-BF) image of a magnetic  
916 ectosymbiotic bacterium detached from its host and (B) single magnetosome chain. (C) High-resolution  
917 transmission electron microscopy (HR-TEM) images of the crystals annotated 1-6 in (B) scale bars 10 nm.  
918 (D) Fast Fourier transform (FFT) patterns of HR-TEM indexed with the magnetite structure (spacegroup  
919  $Fm\bar{3}m$ ,  $a = 8.04 \text{ \AA}$ ). (E) Stereographic projection oriented with respect to the orientation inferred from (D)  
920 using SingleCrystal software, the 111 pole are outlined by a cyan circle. (F) Prismatic models drawn in  
921 white are superimposed to the image of the crystals. Yellow arrows indicate the  $\langle 111 \rangle$  direction: solid  
922 arrows correspond to in-plane direction and dashed arrows are related to out-of-plane direction. The  $\langle 111 \rangle$   
923 directions and the orientation of the models were deduced from the stereographic projections. (G) For each  
924 analyzed crystal, the  $\langle 111 \rangle$  direction is superimposed to the magnetosome chain (red arrows) showing that  
925 their easy magnetization axis is aligned with the overall chain direction.

926



927

928 **Fig. S15. Crystallography of the prismatic/cuboctahedral magnetite particles produced by magnetic**  
 929 **ectosymbiotic bacteria.** (A) TEM-BF image of a magnetic ectosymbiotic bacterium detached from its host.  
 930 (B) HR-TEM images of four crystals with superimposed prismatic models drawn in white and yellow  
 931 arrows to indicate the  $\langle 111 \rangle$  direction (solid arrows are in-plane and dashed arrows out-of-plane). (C) FFT  
 932 pattern of HR-TEM indexed with the magnetite structure (spacegroup  $Fm\bar{3}m$ ,  $a = 8.04 \text{ \AA}$ ). (D)  
 933 Stereographic projection oriented with respect to the orientation inferred from (C) with the 111 pole  
 934 outlined by a cyan circle. (E) For each analyzed crystal, the  $\langle 111 \rangle$  direction is superimposed to the  
 935 magnetosome chain (yellow arrows) showing that their easy magnetization axis is aligned with the overall  
 936 chain direction.

937 **References**

- 938 1. L. Le Nagard, *et al.*, Magnetite magnetosome biomineralization in *Magnetospirillum magneticum*  
939 strain AMB-1: A time course study. *Chem. Geol.* **530**, 119348 (2019).
- 940 2. L. Marcano, *et al.*, Magnetic Anisotropy of Individual Nanomagnets Embedded in Biological  
941 Systems Determined by Axi-asymmetric X-ray Transmission Microscopy. *ACS Nano* (2022)  
942 <https://doi.org/10.1021/acsnano.1c09559>.
- 943 3. A. Isambert, N. Menguy, E. Larquet, F. Guyot, J.-P. Valet, Transmission electron microscopy study  
944 of magnetites in a freshwater population of magnetotactic bacteria. *Am. Mineral.* **92**, 621–630  
945 (2007).
- 946 4. S. Mann, R. B. Frankel, R. P. Blakemore, Structure, morphology and crystal-growth of bacterial  
947 magnetite. *Nature* **310**, 405–407 (1984).
- 948 5. B. Devouard, *et al.*, Magnetite from magnetotactic bacteria: Size distributions and twinning. *Am.*  
949 *Mineral.* **83**, 1387–1398 (1998).
- 950 6. M. Pósfai, C. T. Lefèvre, D. Trubitsyn, D. A. Bazylinski, R. B. Frankel, Phylogenetic significance  
951 of composition and crystal morphology of magnetosome minerals. *Front. Microbiol.* **4**, 344 (2013).

952

953